Research Square

Preprints are preliminary reports that have not undergone peer review.
They should not be considered conclusive, used to inform clinical practice,
or referenced by the media as validated information.

Tissue-specific transcriptomic and ultrastructural responses of the hard clam Meretrix meretrix to suspended sediment stress: insights into molecular defence mechanisms and candidate biomarkers

Xuan Zhang
Chinese Academy of Fishery Sciences
Jingtao Liu
Yancheng Institute of Technology
Haopeng Hu
Chinese Academy of Fishery Sciences
Tianyu Yang
Yancheng Institute of Technology
Mei Jiang
Chinese Academy of Fishery Sciences
Yanming Sui
suiyanming@ycit.edu.cn
Chinese Academy of Fishery Sciences
Lei Li
Chinese Academy of Fishery Sciences

Research Article

Keywords: suspended sediment, Meretrix meretrix, transcriptomics, ultrastructural damage, tissue-specific response, environmental biomarker

Posted Date: November 13th, 2026

DOI: https://doi.org/10.21203/rs.3.rs-11549949/v1

License: This work is licensed under a Creative Commons Attribution 4.0 International License.
Read Full License

Additional Declarations: No competing interests reported.

Tissue-specific transcriptomic and ultrastructural responses of the hard clam *Meretrix meretrix* to suspended sediment stress: insights into molecular defence mechanisms and candidate biomarkers

Xuan Zhang [1], Jingtao Liu [2], Haopeng Hu [1], Tianyu Yang [2], Mei Jiang [1], Yanming Sui [1,2,*] and Lei Li [1,*]

1 Key Laboratory of East China Sea Fishery Resources Exploitation, Ministry of Agriculture and Rural Affairs, East China Sea Fisheries Research Institute, Chinese Academy of Fishery Sciences, Shanghai 200090, China; zhangxuan@ecsf.ac.cn (X. Z.); hu15231265111@163.com (H.H.); jiangrose73@163.com (M.J.); suiyanming@ycit.edu.cn (Y.S.); lilei@ecsf.ac.cn (L.L.).

2 Jiangsu Key Laboratory for Exploration and Utilization of Marine Wetland Biological Resources, Yancheng Institute of Technology, Yancheng 224051, China; liujingtao0819@163.com (J. L.); wqqyty241103@163.com (T.Y.).

* Correspondence: suiyanming@ycit.edu.cn (Y.S.); lilei@ecsf.ac.cn (L.L.).

Abstract

Suspended sediment concentrations (SSCs) in coastal waters have increased due to anthropogenic activities, but the molecular and cellular responses of bivalves remain unclear. Here, we performed combined transcriptomic and ultrastructural analyses on gill and hepatopancreas tissues of the hard clam *Meretrix meretrix* exposed to seven SSC concentrations for 30 days. Transcriptomic analysis revealed tissue-specific responses, with the hepatopancreas exhibiting more DEGs, enriched in energy metabolism, cell death, and immune pathways. Notably, DEG numbers declined at the highest concentration, suggesting adaptive transcriptional suppression. Transmission electron microscopy (TEM) further revealed dose-dependent ultrastructural damage in gill epithelial cells, progressing from early reversible stress to severe necrosis and epithelial barrier collapse. qRT-PCR validated the transcriptomic data, identifying robust candidate biomarkers (e.g., DN88965, DN94928). This study links molecular and cellular responses, providing insights for environmental monitoring in coastal zones.

Keywords: suspended sediment; *Meretrix meretrix*; transcriptomics; ultrastructural damage; tissue-specific response; environmental biomarker.

1. Introduction

Filter feeding bivalves are particularly susceptible to elevated suspended sediment concentrations (SSCs)

because their feeding apparatus—the gill—is in direct and continuous contact with ambient particles [1]. When SSCs exceed natural background levels, physical clogging of gill surfaces, reduced clearance rates, and increased metabolic costs are commonly observed across multiple bivalve species [2]. Anthropogenic activities such as dredging, pipeline laying, and coastal construction are major contributors to acute and chronic SSC elevations in many coastal regions [3], and the spatial overlap between construction generated sediment plumes and bivalve farming grounds has become a growing concern worldwide [4]. In the present study, we used a coastal pipeline construction project in Tongzhou Bay (eastern China) as a realistic scenario for investigating the molecular responses of the hard clam *Meretrix meretrix* to SSC stress. Hydrodynamic simulations for this project predicted SSC increments of 10–150 mg/L above the local background concentration, providing a relevant concentration range for subsequent laboratory exposure experiments.

The hard clam *M. meretrix* (family Veneridae) is one of the most commercially valuable bivalve species along the Chinese coast, supporting large scale aquaculture in intertidal and shallow subtidal zones [5]. As an obligate filter feeder, *M. meretrix* pumps ambient seawater across its gill filaments to retain phytoplankton, organic detritus, and other suspended particles [6]. This feeding mode inevitably exposes its gill tissues—the primary organ for both particle capture and particle rejection—to any suspended particulate matter present in the water column [7]. Elevated SSCs can physically clog the gill sur-face, interfere with particle sorting, induce oxidative stress, and ultimately affect feeding efficiency, energy budget, and organismal fitness [8]. Consequently, the gill serves as the first line of physical defence against SSC stress. Because SSC exposure can also induce metabolic disturbance, oxidative stress, and systemic immune responses, the hepatopancreas represents a complementary and highly informative tissue for investigating the in-ternal molecular responses to sediment stress.

Previous studies have documented adverse effects of elevated SSCs on feeding, growth, and survival in several bivalve species, including the Manila clam Ruditapes philippinarum [9], the Pacific oyster Crassostrea gigas [10], and the blue mussel *Mytilus edulis* [11], and high SSC exposure has caused acute mortality in scallops [12,13]. For *M. meretrix*, however, the molecular and cellular mechanisms underlying SSC stress responses remain largely unexplored. In addition, the structural integrity of the gill epithelium is critical for its barrier and feeding functions, yet the ultrastructural changes induced by SSC stress in this species have not been characterised. Although organism-level endpoints such as growth

and survival are ecologically important, the present study focuses on the molecular and ultrastructural responses of *M. meretrix* to SSC stress.

Recent advances in RNA-sequencing (RNA-seq) have enabled comprehensive transcriptomic profiling of bivalves under various environmental stressors. In *M. meretrix*, sev-eral transcriptomic studies have been conducted, focusing mainly on chemical pollutants. Xu et al. (2024) exposed different developmental stages of *M. meretrix* to cadmium (Cd^{2+}) and identified 31,914 differentially expressed genes (DEGs) involved in oxidative stress, cellular respiration, ion transport, and immune responses [16]. Li et al. (2021) investigated the transcriptomic response of *M. meretrix* to Aroclor 1254 and revealed 5,101 DEGs related to detoxification metabolism, oxidative stress, immune defence, and endocrine disruption [17]. Cao et al. (2019) examined the effects of the organophosphorus pesticide dimethoate and identified 4,119 DEGs [18]. More recently, transcriptomic analyses have been applied to combined thermal and residual chlorine stress [19] and to sodium alginate exposure [20]. Beyond *M. meretrix*, transcriptomic profiling of the Manila clam exposed to contaminated dredged sediments revealed significant transcriptional changes in pathways related to lysosomal function, vesicle trafficking, and mTORC1 signaling [21]. In the abalone Haliotis diversicolor squamata, exposure to total suspended solids induced significant up-regulation of HSP70 and HSP90 genes [22]. However, despite these advances, the molecular pathways that enable clams to tolerate high-sediment environments, and the gene regulatory networks that distinguish physical particle stress from chemical toxicity, remain largely unknown.

To address these knowledge gaps, we conducted a 30-day indoor simulation experiment exposing adult *M. meretrix* to seven SSC concentrations (0, 276, 286, 296, 326, 376, and 426 mg/L), corresponding to the local background SSC and incremental increases above it. We performed transcriptomic profiling (RNA-seq) of gill and hepatopancreas tissues, followed by qRT-PCR validation of selected candidate genes and transmission electron microscopy (TEM) analysis of gill epithelial cells. The specific objectives were: (1) to characterise the genome-wide transcriptomic response of gill and hepatopancreas tis-sues to suspended sediment stress; (2) to identify differentially expressed genes and enriched KEGG pathways associated with physical particle stress; (3) to validate the expression patterns of key candidate genes using qRT-PCR; (4) to evaluate the ultrastructural damage in gill epithelial cells by TEM and link these structural changes with the transcriptomic responses; and (5) to identify potential molecular

biomarkers for environmental monitoring. This study provides a multi-tissue transcriptomic and ultrastructural investigation of SSC stress in *M. meretrix*, focusing on gill and hepatopancreas responses across a realistic SSC gradient and identifying candidate biomarkers for environmental monitoring in coastal construction zones.

2. Materials and Methods

2.1 Experimental Design and Sample Collection

Adult *M. meretrix* were purchased as a single batch from a local seafood market near Tongzhou Bay (Jiangsu, China). Clams were temporarily held in 60-L glass aquaria for 7 days prior to the experiment. During temporary holding period, animals were fed Chlorella vulgaris twice daily (09:00 and 22:00), with residual food and faeces removed before each feeding. Seawater (salinity 27‰, pH 8.23) was renewed daily. The water temperature was maintained at 20 ± 0.5 °C, and dissolved oxygen was kept above 6.0 mg/L by continuous aeration. After the temporary holding period, healthy and active individuals of similar size were selected for the exposure experiment.

The background suspended sediment concentration (SSC) was determined based on the maximum value recorded in the 2025 spring survey (276 mg/L) from the Environmental Impact Assessment Report for the Tongzhou Bay Green Chemical Expansion Zone Tailwater Discharge Pipeline Project (2025). Based on the hydrodynamic predictions from the same report, seven SSC treatments were established at 0, 276, 286, 296, 326, 376, and 426 mg/L. The 0 mg/L treatment (filtered natural seawater) served as the control, while 276 mg/L represented the local background SSC and 286–426 mg/L represented incremental SSC increases above the background. Each treatment was performed in three replicate 60-L aquaria, each containing 40 clams. To ensure uniform particle exposure, clams were placed on custom-made wire mesh platforms within each aquarium. Based on the local tidal cycle (average flood duration 6 h 17 min, average ebb duration 6 h 10 min, total tidal period 12 h 27 min), sediment suspension was generated using wave pumps for 13 h per day, followed by 11 h of quiescence. The exposure lasted for 30 days. Aquaria were randomly assigned to the control and SSC treatment groups using a random number generator. All clams used in this experiment, including the 0 mg/L control and the 276–426 mg/L SSC treatments, were from the same batch and source, and all groups were temporarily held and exposed under identical laboratory conditions.

At the endpoint, three clams per treatment (one from each independent replicate aquarium) were randomly collected. Gill and hepatopancreas tissues were dissected, im-mediately frozen in liquid nitrogen, and stored at −80 °C for RNA extraction and transcriptomic analysis. Clams were handled minimally, and no invasive procedures were performed before terminal sampling.

2.2 Suspended Sediment Preparation, Characterization, and SSC Verification

The suspended sediment used in the exposure experiment was collected in March 2026 from the intertidal mudflat adjacent to the Tongzhou Bay pipeline construction site (Jiangsu, China). After collection, the sediment was air-dried, gently ground, and passed through a 63 μm sieve to remove large particles and debris. The prepared sediment was stored at 4 °C until use.

Particle-size distribution was determined using a laser diffraction particle-size analyzer (Mastersizer 2000, Malvern, UK) after dispersion in sodium hexametaphosphate and ultrasonication. The sediment was composed mainly of sand (78.85%), silt (19.81%), and clay (1.34%). The median grain size was 105.8 μm, the mean particle size was 3.3 φ, and the skewness, kurtosis, and sorting coefficient were −0.16, 1.39, and −1.05, respectively (Table S1).

Experimental seawater was prepared as artificial seawater at a salinity of 27‰ and pH 8.23. The concentrations of inorganic nitrogen, phosphate, and COD were 226 μg/L, 22.5 μg/L, and 2.01 mg/L, respectively (Table S2). These water-quality parameters were determined according to the Specification for Marine Monitoring (GB 17378-2007).

SSC stock suspensions were prepared by adding a known mass of the prepared sediment to filtered natural seawater, followed by vigorous mixing. Seven target SSC treatments were established as described in Section 2.1. During the 30-day exposure, actual SSC concentrations were verified once daily by gravimetric analysis. A known volume of water was filtered through a pre-weighed GF/F filter, dried at 105 °C to constant weight, and the SSC was calculated as the dry weight of retained sediment per unit volume of water (mg/L). A portable turbidity meter, calibrated against the gravimetric measurements, was used for real-time monitoring. When the measured SSC deviated from the target con-centration by more than ±10%, additional sediment or seawater was added to restore the target concentration.

2.3 Transmission Electron Microscopy (TEM)

The fixed samples were washed three times with 0.1 M phosphate buffer (pH 7.0) for 15 min each. Subsequently, the samples were post-fixed in 1% osmium tetroxide for 1–2 h. After carefully removing the osmium tetroxide waste, the samples were washed again three times with 0.1 M phosphate buffer (pH 7.0) for 15 min each. The samples were then dehydrated in a graded ethanol series (30%, 50%, 70%, 80%, 90%, and 95%) for 15 min at each concentration, followed by two treatments with 100% ethanol for 20 min each, and finally transferred to pure acetone for 20 min. For infiltration, the samples were treated with a mixture of embedding medium and acetone (V/V = 1:1) for 1 h, then with a mixture of embedding medium and acetone (V/V = 3:1) for 3 h, and finally with pure embedding medium overnight. The infiltrated samples were embedded and polymerized at 70 °C overnight. Ultrathin sections (70–90 nm) were cut using an ultramicrotome and stained with lead citrate and uranyl acetate (50% ethanol saturated solution) for 5–10 min each. After drying, the sections were examined using a Hitachi HT7800 transmission electron microscope (Hitachi, Tokyo, Japan) at an accelerating voltage of 80 kV. Images were captured at a magnification of 6000×. For semiquantitative analysis, five individuals per group were examined. Five ultrastructural indicators (nuclear morphology, mitochondrial structure, cytoplasmic vacuolization, ciliary integrity, and intercellular junction condition) were scored from 0 (no damage) to 4 (severe necrotic damage). The mean score across the five indicators was used for statistical analysis.

2.4 RNA Extraction, Library Construction, and Sequencing

Total RNA was extracted from gill tissues and hepatopancreas tissues (three biological replicates per treatment; 30 days post-exposure) using TRIzol® Reagent (Invitrogen, USA) according to the manufacturer's instructions. RNA purity was assessed using a NanoPhotometer® spectrophotometer (IMPLEN, USA), and RNA concentration was measured using a Qubit® RNA Assay Kit with a Qubit® 2.0 Fluorometer (Life Technologies, USA). RNA integrity was evaluated using the RNA Nano 6000 Assay Kit on an Agilent Bioanalyzer 2100 system (Agilent Technologies, USA). Only samples with RNA integrity number (RIN) values ≥ 8.0 were used for library construction.

Sequencing libraries were constructed using the TruSeq™ RNA Sample Prep Kit (Il-lumina, USA) following the manufacturer's recommendations. Briefly, mRNA was purified from total RNA using oligo(dT)-attached magnetic beads (Invitrogen, USA) and fragmented into short pieces using ultrasound. First-strand cDNA was synthesised using random hexamer primers and MMuLV Reverse Transcriptase. Second-strand cDNA syn-thesis was subsequently performed using DNA Polymerase I and RNase H.

The dou-ble-stranded cDNA fragments were subjected to end-repair, adenylation of the 3′ ends, and ligation of sequencing adapters. The library fragments were purified with the AMPure XP system (Beckman Coulter, USA) to select cDNA fragments of approximately 200–300 bp in length, followed by PCR amplification and a second purification step using AMPure XP beads. Library quality was assessed on the Agilent Bioanalyzer 2100 system.

After cluster generation on a cBot Cluster Generation System using the TruSeq PE Cluster Kit v3-cBot-HS (Illumina, USA), the library preparations were sequenced on an Il-lumina NovaSeq 6000 platform (Illumina, USA) using the TruSeq SBS Kit (300 cycles), generating 150 bp paired-end reads.

The raw sequencing reads generated in this study have been deposited in the NCBI Sequence Read Archive (SRA) and are accessible through BioProject accession number PRJNA1509981.

2.5 Transcriptome Assembly and Annotation

2.5.1 Quality Control and De Novo Assembly

Raw sequencing reads in FASTQ format were processed using Trimmomatic v0.39 [23]. Reads containing adapters, reads containing poly-N sequences, and low-quality reads (Qscore ≤ 20) were removed, generating clean reads. The Q20, Q30, and GC content of the clean data were calculated. All downstream analyses were based on the clean, high-quality reads.

Transcriptome assembly was performed using Trinity v2.15.2 [24] with default parameters. The resulting transcripts were clustered into unigenes using Corset [25] with default parameters. Transcript length distribution, N50, and total number of assembled transcripts were reported. Clean reads were aligned to the assembled transcriptome using Salmon v1.10.1 [26]. Assembly completeness was assessed using BUSCO v6.1.0 with the lophotrochozoa_odb12.2 lineage dataset in eukaryotic transcriptome mode (euktran). In addition, clean reads were mapped back to the assembled unigenes using HISAT2 v2.2.1, and the overall alignment rate was calculated to evaluate assembly completeness.

2.5.2 Functional Annotation

Unigenes were annotated against the following public databases using Diamond v2.1.11 （BLASTX, E value < 1×10^{-5}）: NCBI NR (Non Redundant Protein Database) [27], KEGG （Kyoto Encyclopedia of Genes and Genomes） [28], and Swiss Prot [29]. eggNOG and GO annotations were performed using

eggnog mapper v5.0 [30]. Open reading frames (ORFs) were predicted using TransDecoder v5.5.0 [31].

2.6 Differential Expression Analysis

Transcript-level estimated counts were generated using Salmon v1.10.1 [26] and im-ported into R using txiimport. Differential expression analysis was performed using the R package edgeR v3.6.3 [32] in R v3.6.3 based on the estimated counts. Genes with $|\log_2(\text{fold change})| \geq 1$ and false discovery rate (FDR) < 0.05 were considered differentially expressed genes (DEGs). TPM values were used only for descriptive visualization, including expression distribution plots and clustering heatmaps.

To visualise sample relationships, principal component analysis (PCA) was per-formed using R v3.6.3, and sample clustering and correlation analyses were conducted using the same software. Venn diagrams of DEGs among treatment groups were generated using the VennDiagram R package.

2.7 Functional Enrichment Analysis

GO enrichment analysis of DEGs was performed using GOTools v0.9.9 [33] with a hypergeometric test and Benjamini Hochberg false discovery rate (FDR) correction. GO terms with FDR < 0.05 were considered significantly enriched.

KEGG pathway enrichment analysis was performed using KOBAS v3.0 [34], with FDR < 0.05 as the significance threshold. Enriched pathways were visualised using dot plots and pathway maps.

2.8 Expression Pattern Clustering

Expression pattern clustering of DEGs across treatments was performed using R v3.6.3 with the soft clustering method, and genes sharing similar temporal expression profiles were grouped into clusters for functional interpretation.

2.9 Quantitative Real Time PCR (qRT PCR) Validation

To validate the RNA-seq results, 12 DEGs were selected for qRT-PCR analysis. Total RNA (1 μg) was reverse-transcribed using the PrimeScript™ RT Reagent Kit with gDNA Eraser (RR047A, Takara, Japan) according to the manufacturer's protocol. qRT-PCR was performed using Vazyme qPCR Mix (Q321, Vazyme, China) on an ABI 7500 Real-Time PCR System (Applied Biosystems, USA). The reaction mixture (30 μL) contained 15 μL of qPCR Mix, 0.5 μL each of forward and reverse primers (10 μM), 2

μL of template DNA, and ddH_2O to a final volume of 30 μL. The cycling conditions were: 95 °C for 3 min, followed by 40 cycles of 95 °C for 15 s, 57 °C (or 62 °C for 18S rRNA, DN145, DN44109, and DN88965) for 20 s, and 72 °C for 20 s. A melt curve analysis was performed to verify the specificity of each amplicon. Each biological replicate was assessed with three technical replicates, and three biological replicates were included per treatment (n = 3). The 2^−ΔΔCt method [35] was used to calculate relative expression levels, with 18S rRNA as the internal reference gene and the 0 mg/L group as the calibrator. For statistical analysis, the three technical replicates were averaged for each biological replicate, and data are presented as mean ± standard deviation (SD). Normality and homogeneity of variance were assessed using the Shapiro–Wilk test and Levene's test, respectively. Differences in relative expression between the 426 mg/L treatment and the 0 mg/L control were analysed using independent-sample t-tests. When normality or variance homogeneity was not met, the non-parametric Mann–Whitney U test was used. A p-value < 0.05 was considered statistically significant. Pearson correlation analysis was performed between RNA-seq $\log_2$ fold changes and $\log_2$-transformed qRT-PCR relative expression values (2^−ΔΔCt) using SPSS v25.0 (IBM, USA). The correlation coefficient (r) and p-value were calculated for all 12 genes and for the 9 genes excluding the three discordant ones (DN37274, DN41008, and DN57710). Primer sequences, annealing temperatures, and the results of the correlation analysis are listed in Supplementary Table S3.

2.10 Statistical Analysis

Transcriptome statistical analyses were performed as described in the respective sections above. All data were expressed as mean ± standard deviation (SD) where applicable.

3. Results

3.1 Transcriptome Sequencing and De Novo Assembly

3.1.1 Sequencing Data Quality Control and Assembly

To obtain a comprehensive transcriptomic profile of *M. meretrix* in response to SSC stress, a total of 42 cDNA libraries were constructed from gill and hepatopancreas tissues (seven treatments: 0, 276, 286, 296, 326, 376, and 426 mg/L SSC; three biological replicates per treatment per tissue) and sequenced on the Illumina NovaSeq 6000 platform, generating a total of 1.91 billion raw reads. After quality filtering, a total of 1.89 billion clean reads were retained, with an average of 44.95 million clean reads per sample.

The Q20 and Q30 values of the clean reads exceeded 98.70% and 95.55%, respectively, across all samples, indicating high-quality sequencing data. GC content ranged from 33.85% to 37.63% across samples (Table 1).

De novo assembly of the clean reads yielded 277,335 transcripts with an N50 of 746 bp. These transcripts were further clustered to generate 154,845 non-redundant unigenes, with a total length of 111,021,589 bp and an average length of 716.99 bp. The largest unigene was 14,920 bp (Table 1). BUSCO assessment showed that 73.2% of conserved lophotrochozoan genes were complete (single-copy: 70.5%; duplicated: 2.7%), 16.3% were fragmented, and 10.5% were missing (n = 1,329). In addition, clean reads were mapped back to the assembled unigenes, with an overall alignment rate ranging from 68.51% to 87.33% across all 42 samples (average: 74.64%). These mapping rates indicate that the assembled transcriptome captured a substantial proportion of the expressed transcripts and was suitable for downstream differential expression analysis. These assembly statistics indicate that the transcriptome assembly was of sufficient quality for downstream functional annotation and differential expression analysis.

Table 1. Summary of RNA-seq data quality control and assembly statistics.

Category	Metric	Value
Sequencing	Total raw reads	1.91 billion
	Total clean reads	1.89 billion
	Average clean reads per sample	44.95 million
	Q20 (%)	> 98.70
	Q30 (%)	> 95.55
	GC content range (%)	33.85 – 37.63
Assembly	Total unigenes	154,845
	Total isoforms	277,335
	Total unigene length (bp)	111,021,589
	Average unigene length (bp)	716.99
	N50 (bp)	746

Category	Metric	Value
	Largest unigene (bp)	14,920
Assembly completeness	BUSCO complete (%)	73.2
	BUSCO fragmented (%)	16.3
	BUSCO missing (%)	10.5
Read mapping	Overall mapping rate (%)	68.51–87.33 (avg. 74.64)

3.1.2 Functional Annotation

To assign putative functions to the assembled unigenes, all 154,845 unigenes were searched against the NR, GO, eggNOG, KEGG, Swiss Prot, and CAZy databases. Among these, 40,306 unigenes (26.03%) were successfully annotated in the NR database, which had the highest annotation rate. Annotation rates for other databases were as follows: eggNOG (27,494; 17.76%), KEGG (26,090; 16.85%), GO (18,321; 11.83%), Swiss Prot (17,722; 11.45%), and CAZy (1,555; 1.00%) (Table 2). The relatively low overall annotation rate is typical for de novo transcriptomes of non-model organisms and reflects the limited availability of closely related genomic resources. Nevertheless, the annotated unigenes provided sufficient coverage for subsequent functional enrichment analyses. Open reading frames (ORFs) were predicted, identifying 34,392 putative ORFs.

Table 2. Functional annotation statistics of assembled unigenes.

Database	Annotated Unigenes	Percentage (%)
NR	40,306	26.03
eggNOG	27,494	17.76
KEGG	26,090	16.85
GO	18,321	11.83
Swiss-Prot	17,722	11.45

Database	Annotated Unigenes	Percentage (%)
CAZy	1,555	1.00

3.1.3 Gene Expression Profiles and Sample Relationships

The distribution of gene expression levels across all samples was visualised using density plots and boxplots of $\log_2$(TPM+1) values (Figure 1A–B). The density curves showed that the majority of genes exhibited low to moderate expression levels across all treatments, with a unimodal distribution peaking around $\log_2$(TPM+1) = 2–3. The boxplot analysis revealed similar median expression levels across all samples, with comparable interquartile ranges and overall distributions.

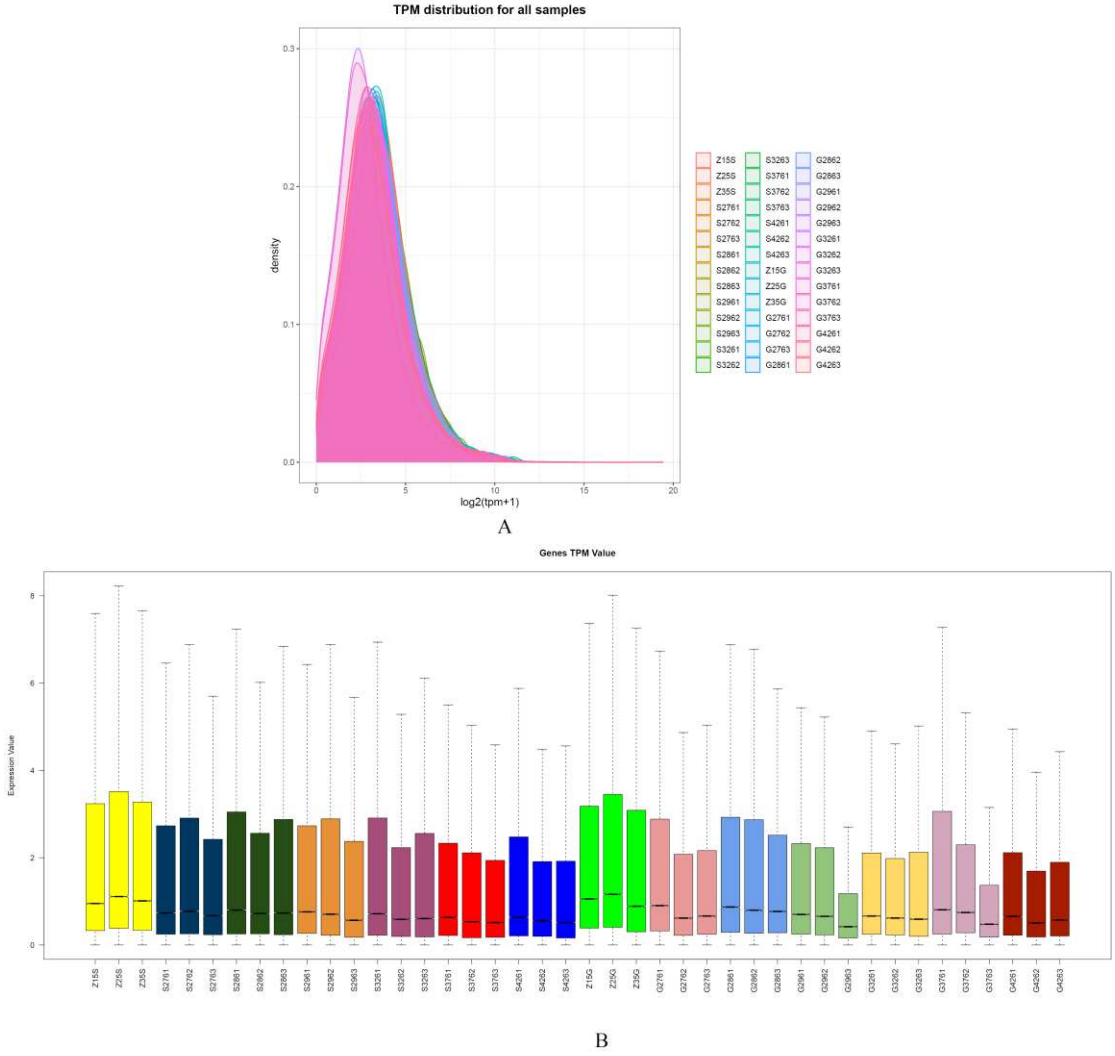


Figure 1. Gene expression profiles across all samples. (A) Density plot of $\log_2$(TPM+1) values showing the

distribution of gene expression levels. (B) Boxplot of $\log_2$(TPM+1) values across 42 samples. Boxes represent the interquartile range, horizontal lines indicate medians, and whiskers extend to 1.5 × IQR.

Principal component analysis (PCA) of the transcriptomic profiles revealed that PC1 and PC2 explained 17.78% and 13.36% of the total variance, respectively (Figure 2A). The PCA plot showed clear separation between the 0 mg/L control group and all SSC treated samples along PC1, with the 426 mg/L treatment showing the greatest divergence from the control. Samples from the same treatment group clustered closely together, indicating high reproducibility among biological replicates.

Hierarchical clustering analysis further confirmed that samples grouped primarily by treatment, with all biological replicates within each treatment forming distinct clusters (Figure 2B). Sample correlation analysis showed Pearson correlation coefficients exceeding 0.80 among biological replicates within the same treatment group, while correlations be-tween different treatment groups decreased with increasing concentration differences (Figure 3). These results demonstrate that SSC exposure induced concentration dependent transcriptomic reprogramming in *M. meretrix*, and the high reproducibility within treatment groups supports the reliability of the transcriptomic data for downstream differential expression analysis.

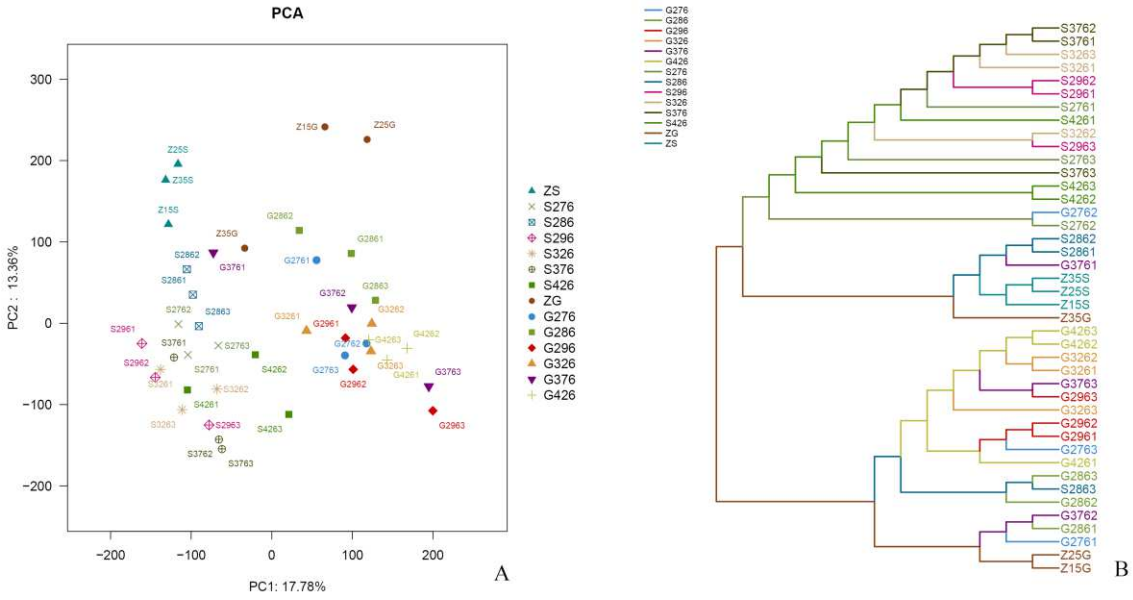


Figure 2. Sample relationship analysis. (A) PCA plot of all samples; PC1 and PC2 explained 17.78% and 13.36% of the variance, respectively. (B) Hierarchical clustering dendrogram based on Pearson correlation coefficients. (C) Correlation heatmap showing pairwise Pearson correlation coefficients among all samples (red: high correlation; blue: low correlation).

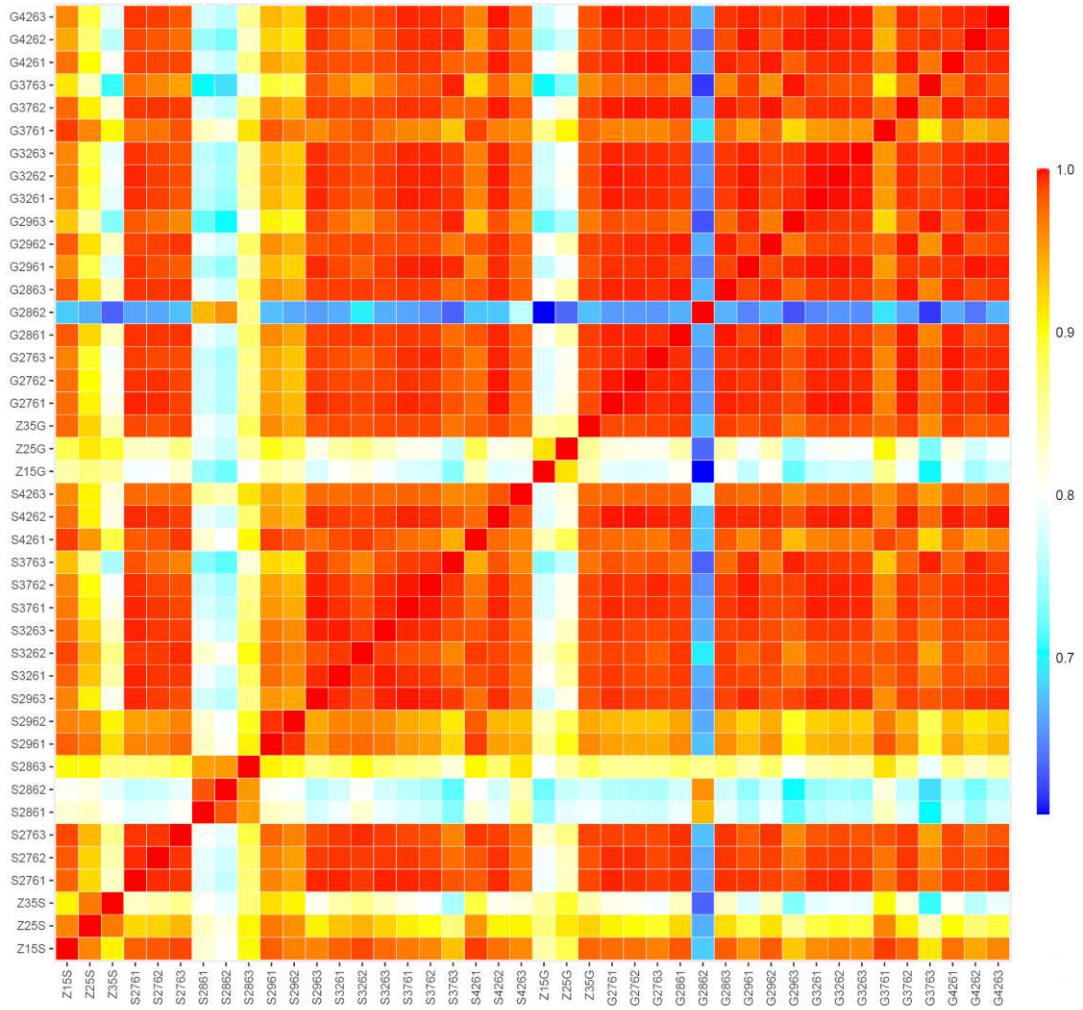


Figure 3. Sample relationship analysis. Correlation heatmap showing pairwise Pearson correlation coefficients among all samples (red: high correlation; blue: low correlation).3.2 Ultrastructural Alterations of Gill Epithelial Cells Under Different SSC Concentrations

3.2.1 Control Group

The gill epithelial cells in the control group maintained well-preserved ultrastructure (Figure 4A). The nuclei were oval-shaped, with continuous and smooth double-layered nuclear membranes and evenly distributed chromatin. No chromatin aggregation, margination, nuclear membrane folding or rupture was observed.

In the cytoplasm, mitochondria were plump with clear and intact cristae, and organelles such as the endoplasmic reticulum were arranged in an orderly manner. Cell boundaries were distinct, intercellular junctions remained intact, and intercellular spaces showed no obvious dilation. Only a small number of

physiological vesicles were detected in the cytoplasm, without extensive vacuolization, cytoplasmic lysis or accumulation of abundant autophagolysosomes. The cilia on the apical surface of the gill epithelium were neatly arranged and structurally complete. A few bright white cavities in the sections were artifacts generated during resin embedding and ultrathin sectioning, and did not represent tissue or cell damage.

3.2.2 Ultrastructural Damage in SSC Treatment Groups

Compared with the control group, gill epithelial cells in all SSC treatment groups exhibited different degrees of ultrastructural damage, and the severity of damage gradually increased with rising SSC concentration.

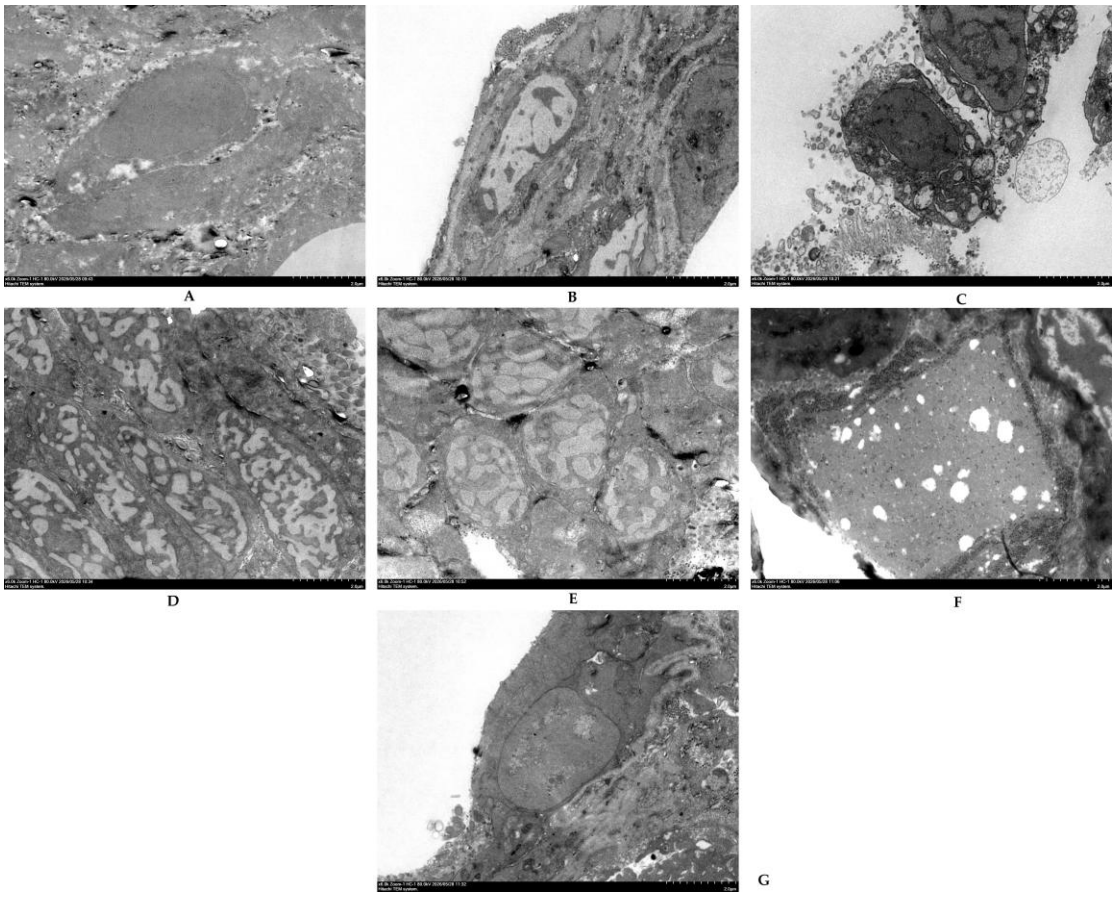


Figure 4. Transmission electron micrographs of gill epithelial cells in *M. meretrix* exposed to different concentrations of suspended solids (SSC). (A) Control group, with intact epithelial structure, regular nuclei, evenly distributed chromatin, well-organized organelles and intact intercellular junctions. (B) 276 mg/L SSC group, showing early stress damage including local chromatin margination, mild mitochondrial swelling, increased cytoplasmic vesicles and disorganized cilia. (C) 286 mg/L SSC group, with moderate damage including extensive ciliary shedding, chromatin aggregation and margination, swollen mitochondria with fractured cristae, aggravated

cytoplasmic vacuolization and widened intercellular spaces. (D) 296 mg/L SSC group, showing moderate-to-severe damage with highly aggregated chromatin in clumps, extensively vacuolated mitochondria, and loosened intercellular junctions. (E) 326 mg/L SSC group, with severe damage including folded and partially discontinuous nuclear membrane, almost completely dissolved mitochondrial cristae, widespread cytoplasmic lysis and disorganized epithelial structure. (F) 376 mg/L SSC group, showing near-terminal destruction with indistinct nuclear membrane, totally disintegrated organelles, completely ruptured intercellular junctions and fully disorganized epithelial layer. (G) 426 mg/L SSC group, with terminal necrotic damage including nuclear pyknosis and karyolysis, completely disintegrated organelles, abundant myelin figures and totally collapsed epithelial structure. Scale bars: A–G = 2 μm. Bright white cavities are artifacts from section preparation.

276 mg/L SSC group： Early stress damage was detected in epithelial cells (Figure 4B). Some nuclei showed slight deformation with local chromatin aggregation and margination. Partial mitochondria presented mild swelling, with sparse and locally fractured cristae. The number of vesicles in the cytoplasm increased significantly, with scattered vacuolization. Intercellular spaces were slightly widened, while intercellular junctions remained largely intact. The cilia on the epithelial surface were locally disorganized. Overall, the damage was mild and appeared to represent an early, likely reversible cellular stress response.

286 mg/L SSC group： Cellular damage was significantly aggravated compared with the 276 mg/L group (Figure 4C). Cilia on the gill epithelial surface were extensively shed and scattered, indicating obvious structural destruction of cilia. Nuclei were irregular in shape, with widespread chromatin aggregation and margination, and nuclear membrane folding was observed in some cells. Mitochondrial swelling was exacerbated, with massive cristae fracture and dissolution. The number of vacuoles and vesicles in the cytoplasm increased markedly, and autophagosome-like structures were visible. The cytoplasmic matrix showed locally uneven electron density. Intercellular spaces were further widened, cell boundaries were partially blurred and discontinuous, and numerous vesicles and cell debris were present around cells. These changes likely impaired the integrity of the gill epithelial barrier.

296 mg/L SSC group： Gill epithelial damage continued to worsen and entered a moderate-to-severe stage (Figure 4D). Chromatin was highly aggregated into coarse clumps and marginated along the nuclear envelope, with large loose vacuolated areas inside the nucleus. The nuclear membrane was extremely irregular with obvious folding. Mitochondria were generally severely swollen, with extensively dissolved

cristae and a mostly vacuolated appearance. The endoplasmic reticulum was significantly dilated into vesicular structures. Numerous large vacuoles and increased autophagic vesicles were distributed in the cytoplasm, accompanied by decreased electron density of the cytoplasmic matrix and enhanced lytic appearance. Intercellular spaces were markedly dilated, most intercellular junctions were loosened, cell boundaries were blurred, and the continuity of the epithelial layer was further impaired.

326 mg/L SSC group: Cells showed severe ultrastructural damage (Figure 4E). Chromatin was highly aggregated and marginated, with large vacuolated areas inside the nucleus. The nuclear membrane was severely irregular with multiple folds and depressions, as well as locally blurred and discontinuous boundaries, showing an obvious tendency of nuclear pyknosis. Mitochondria were extensively and severely vacuolated, with cristae almost completely dissolved. The endoplasmic reticulum was highly dilated into large vesicles. The cytoplasm was filled with vacuoles of various sizes and autophagic vesicles, and the electron density of the cytoplasmic matrix decreased sharply. This presented widespread lysis and obvious organelle disintegration. Intercellular spaces were remarkably expanded, intercellular junctions were nearly ruptured, most cell boundaries were blurred, and the epithelial layer was structurally disorganized. Abundant cell debris was visible around cells, resulting in severe impairment of gill epithelial barrier function.

376 mg/L SSC group: Damage further deteriorated to near-terminal destruction (Figure 4F). The nuclear membrane boundary was indistinct, and the nucleocytoplasmic boundary disappeared. Chromatin was highly condensed and pyknotic, and local nuclear membrane rupture was observed. The nucleus was severely distorted, and its structural integrity was profoundly compromised. Mitochondria were completely vacuolated with cristae totally lost. Membranous organelles such as the endoplasmic reticulum were extensively disintegrated. The cytoplasm was filled with vacuoles, vesicles and cell debris of various sizes, and the cytoplasmic matrix was severely lysed with significantly reduced electron density. Intercellular spaces were extremely dilated, intercellular junctions were completely ruptured, and cell boundaries were barely recognizable. The epithelial layer was fully disorganized, and the interstitial space was filled with cell debris and shed vesicles, resulting in complete loss of gill epithelial structure and barrier function.

426 mg/L SSC group: The most severe terminal necrotic damage was observed at the highest concentration (Figure 4G). Nuclei showed severe pyknosis with highly condensed and marginated

chromatin. Nuclear membrane rupture and karyoplasm leakage occurred in some cells, resulting in karyolysis and complete destruction of nuclear structure. Organelles including mitochondria and the endoplasmic reticulum were completely disintegrated. The cytoplasm was filled with numerous vacuoles, lysosomal residues and cell debris, and abundant myelin figures formed by membrane breakdown were visible. These structures are typical features of cell necrosis. Intercellular junctions disappeared completely, cell boundaries were unidentifiable, and the epithelial structure was totally collapsed. Cilia on the apical surface were completely shed, and the interstitial space was filled with disintegration products, leading to complete loss of gill epithelial structure and function.

3.2.3 Semiquantitative Scoring of Ultrastructural Damage

To quantify the severity of ultrastructural lesions, a 5-point semiquantitative scoring system was adopted. Five core indicators were evaluated: nuclear morphology, mitochondrial structure, cytoplasmic vacuolization, ciliary integrity, and intercellular junction condition. Each indicator was scored on a scale of 0 (no damage) to 4 (severe necrotic damage). The mean score across the five indicators was calculated for each individual (n = 5 per group).

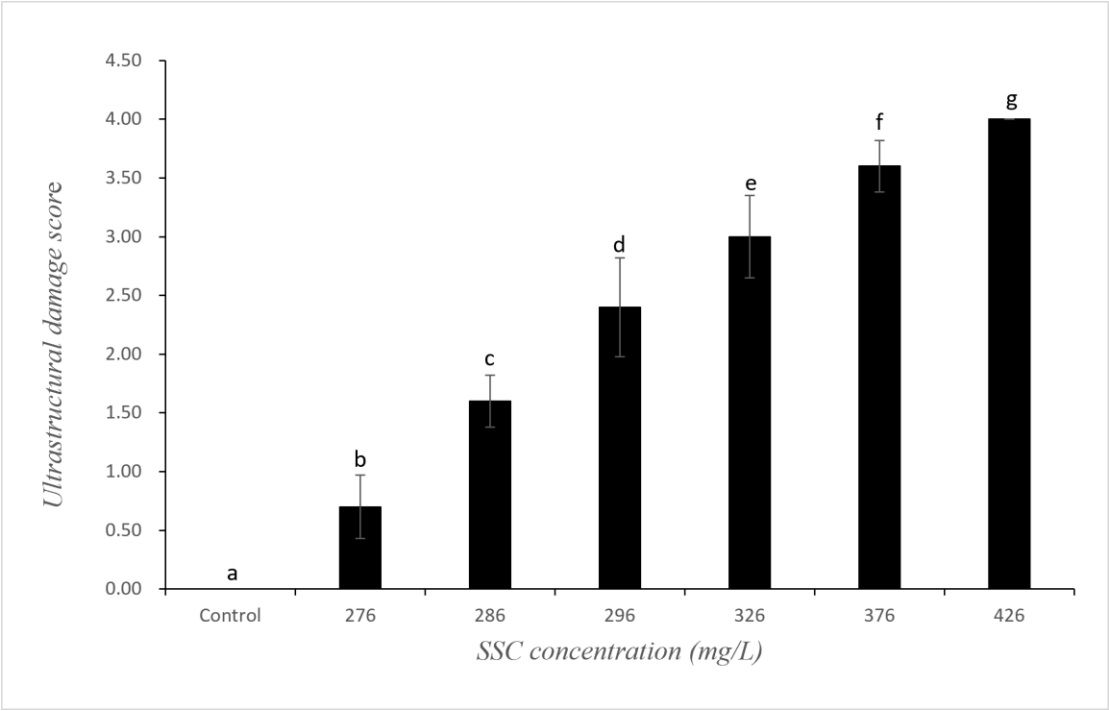


Figure 5. Semiquantitative scores of ultrastructural damage in gill epithelial cells of *M. meretrix* under different SSC concentrations (n = 5, Mean ± SD). Different lowercase letters indicate significant differences between groups

(Duncan's test, $P < 0.05$).

One-way analysis of variance (ANOVA) demonstrated a highly significant main effect of SSC concentration on the mean damage score ($F = 163.684$, $df = 6, 28$, $P < 0.001$). Duncan's multiple range test was performed for post hoc pairwise comparisons. The results showed that all groups differed significantly from each other ($P < 0.05$; Figure 5).

The mean damage score increased progressively with increasing SSC concentration. The control group had the lowest score (0.00 ± 0.00). Scores rose to 0.70 ± 0.27 at 276 mg/L, 1.60 ± 0.22 at 286 mg/L, 2.40 ± 0.42 at 296 mg/L, 3.00 ± 0.35 at 326 mg/L, and 3.60 ± 0.22 at 376 mg/L. The highest score (4.00 ± 0.00) was observed in the 426 mg/L group.

3.2.4 Concentration-Dependent Damage Pattern

Consistent with morphological observations and semiquantitative scoring, the ultrastructural damage of gill epithelial cells in *M. meretrix* showed a clear concentration-effect relationship within the range of 276–426 mg/L SSC.

Low-concentration stress (276 mg/L) only induced early cellular stress responses that appeared to be reversible, with damage limited to mild organelle lesions and ciliary disorganization. At 286 mg/L, damage was markedly upgraded to a moderate stage. Ciliary shedding, cytoplasmic vacuolization and intercellular junction loosening were all significantly intensified. At 296 mg/L, damage developed to a moderate-to-severe stage, and likely irreversible lesions of the nucleus and organelles began to emerge. The 326 mg/L and 376 mg/L groups progressed to severe damage and pre-terminal damage, respectively, with stepwise deterioration of nuclear membrane integrity, organelle disintegration and epithelial barrier failure. At the highest concentration of 426 mg/L, cells exhibited complete necrotic disintegration with abundant myelin figures, and the epithelial structure was completely destroyed.

These results indicate that SSC stress induces dose-dependent ultrastructural damage in gill epithelial cells of *M. meretrix*. Low concentrations mainly trigger cellular stress responses, while high concentrations tend to cause irreversible cell necrosis and epithelial structural collapse.

3.3 Differential Expression Analysis

To identify genes responsive to SSC stress, differential expression analysis was per-formed between each

SSC treatment (276, 286, 296, 326, 376, and 426 mg/L) and the 0 mg/L control using the R package edgeR. Genes with $|\log_2(\text{fold change})| \geq 1$ and FDR < 0.05 were considered differentially expressed genes (DEGs). The numbers of DEGs identified in gill and hepatopancreas tissues are summarised in Table 3.

Table 3. Numbers of differentially expressed genes (DEGs) in gill and hepatopancreas tissues of *M. meretrix* exposed to different SSC concentrations for 30 days ($|\log_2 FC| \geq 1$, FDR < 0.05).

Tissue	Comparison	Total DEGs	Up-regulated	Down-regulated
Gill	276 vs 0	1494	950	544
	286 vs 0	791	372	419
	296 vs 0	1159	521	638
	326 vs 0	1235	624	611
	376 vs 0	1549	909	640
	426 vs 0	1004	612	392
Hepatopancreas	276 vs 0	1775	763	1012
	286 vs 0	2077	1083	994
	296 vs 0	1896	656	1240
	326 vs 0	2567	1406	1161
	376 vs 0	2002	806	1196
	426 vs 0	2003	1085	918

In the gill tissue, the number of DEGs varied across SSC concentrations in a fluctuated pattern (Figure 6A-F). The lowest number of DEGs was observed at 286 mg/L (791 DEGs), while the highest was at 376 mg/L (1549 DEGs). Intriguingly, at the highest con-centration (426 mg/L), the number of DEGs decreased to 1004, lower than that observed at 296 and 326 mg/L. The highest proportion of up-regulated genes was observed at 276 mg/L (950 up-regulated, 63.6% of total DEGs).

In the hepatopancreas tissue, the number of DEGs was substantially higher than in the gill across all treatments (Figure 7A-F), indicating a more pronounced transcriptional response in this metabolic organ.

The number of DEGs ranged from 1775 (276 vs 0) to 2567 (326 vs 0). The highest number of DEGs was observed at 326 mg/L (2567 DEGs), which was also the peak concentration for up-regulated genes (1406). In contrast to the gill, down-regulated genes generally outnumbered up-regulated genes in most comparisons (276, 296, and 376 mg/L), with the exception of the 286, 326, and 426 mg/L treatments where up-regulated genes were more abundant. This difference between tissues suggests that the gill and hepatopancreas may employ distinct transcriptional strategies in response to SSC stress: the gill tends toward activation of stress responsive genes, while the hepatopancreas exhibits a more complex response involving both activation and repression of distinct gene sets.

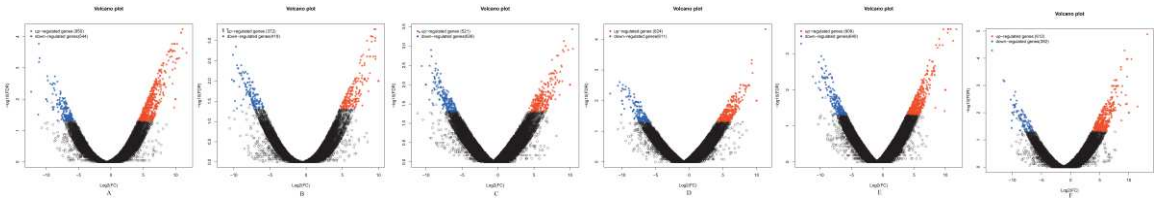


Figure 6. Volcano plots of DEGs in gill and hepatopancreas tissues across SSC treatments versus the 0 mg/L control. (A) Gill, 276 vs 0; (B) Gill, 286 vs 0; (C) Gill, 296 vs 0; (D) Gill, 326 vs 0; (E) Gill, 376 vs 0; (F) Gill, 426 vs 0; (G) Hepatopancreas, 276 vs 0; (H) Hepatopancreas, 286 vs 0; (I) Hepatopancreas, 296 vs 0; (J) Hepatopancreas, 326 vs 0; (K) Hepatopancreas, 376 vs 0; (L) Hepatopancreas, 426 vs 0. Red and blue dots indicate significantly up and down regulated genes, respectively ($|\log_2 FC| \geq 1$, FDR < 0.05); grey dots represent non-DEGs. Numbers in each panel indicate total DEGs identified in that comparison.

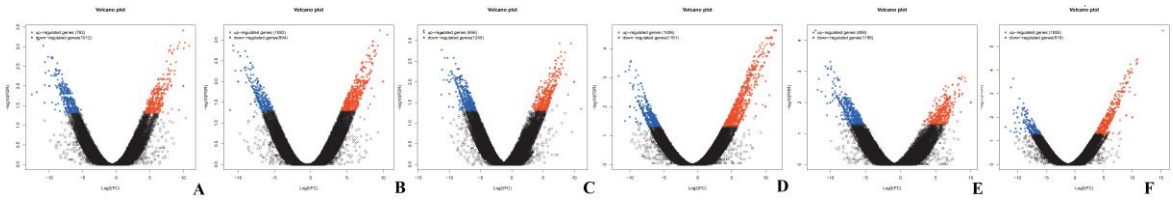


Figure 7. Volcano plots of DEGs in gill and hepatopancreas tissues across SSC treatments versus the 0 mg/L control. (A) Hepatopancreas, 276 vs 0; (B) Hepatopancreas, 286 vs 0; (C) Hepatopancreas, 296 vs 0; (D) Hepatopancreas, 326 vs 0; (E) Hepatopancreas, 376 vs 0; (F) Hepatopancreas, 426 vs 0. Red and blue dots indicate significantly up and down regulated genes, respectively ($|\log_2 FC| \geq 1$, FDR < 0.05); grey dots represent non-DEGs. Numbers in each panel indicate total DEGs identified in that comparison.

3.4 Expression Pattern Clustering

To visualise the expression dynamics of DEGs across different SSC concentrations, hierarchical

clustering analysis was performed on all DEGs identified in gill and hepato-pancreas tissues. The heatmap in Figure 4 displays the log_2(TPM+1) expression values of DEGs across all seven treatment groups (0, 276, 286, 296, 326, 376, and 426 mg/L) for both tissues (Figure 8, Figure 9).

In the hepatopancreas, a clear separation of samples by treatment group was observed, with biological replicates within each treatment clustering together, confirming the reproducibility of the transcriptomic data. DEGs in the hepatopancreas exhibited distinct expression patterns across the SSC gradient. A subset of genes showed progressive up regulation with increasing SSC concentrations, particularly at 326 and 426 mg/L, while another subset displayed gradual down regulation, especially at 296 and 376 mg/L. Notably, the 0 mg/L control samples formed a distinct cluster separate from all SSC treated groups, indicating substantial transcriptional reprogramming induced by SSC exposure. In the gill tissue, similar hierarchical clustering patterns were observed, though the overall number of DEGs was lower than in the hepatopancreas.

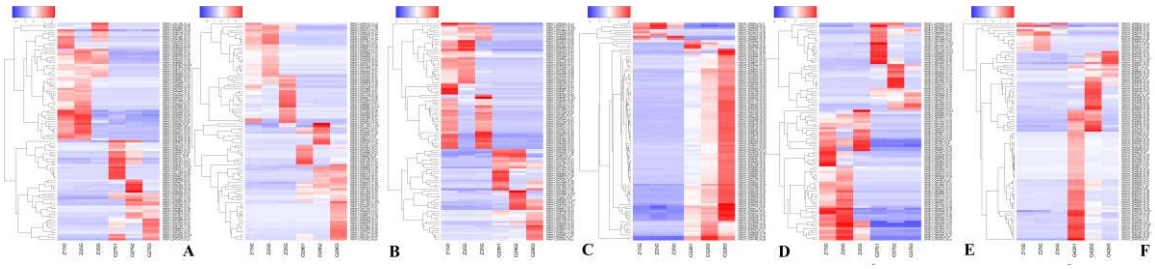


Figure 8. Hierarchical clustering heatmap of DEGs in hepatopancreas and gill tissues across all SSC treatments. Rows represent individual genes, and columns represent samples. The colour scale indicates log_2(TPM+1) expression levels (red: high expression; blue: low expression). The dendrograms on the left and top represent gene and sample clustering, respectively. Sample labels: Z, 0 mg/L control; S, gill; G, hepatopancreas; numbers indicate SSC concentrations (e.g., S2761 = gill, 276 mg/L, replicate 1; G4263 = hepatopancreas, 426 mg/L, replicate 3).

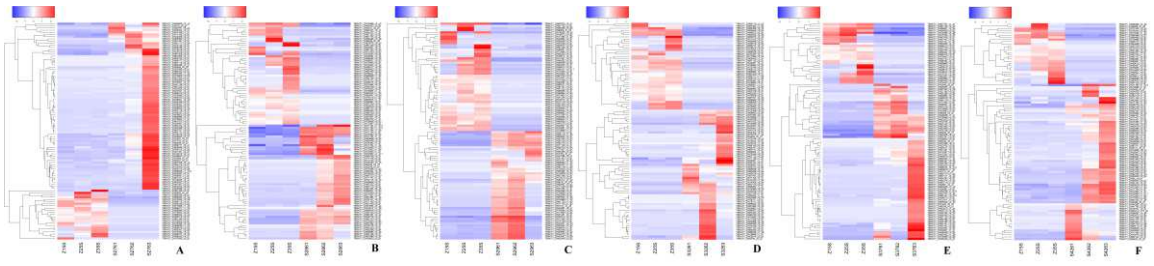


Figure 9. Hierarchical clustering heatmap of DEGs in hepatopancreas and gill tissues across all SSC treatments. Rows represent individual genes, and columns represent samples. The colour scale in-dicates log_2(TPM+1)

expression levels (red: high expression; blue: low expression). The dendrograms on the left and top represent gene and sample clustering, respectively. Sample labels: Z, 0 mg/L control; S, gill; G, hepatopancreas; numbers indicate SSC concentrations (e.g., S2761 = gill, 276 mg/L, replicate 1; G4263 = hepatopancreas, 426 mg/L, replicate 3).

3.5 Venn Analysis of DEGs

To investigate the specificity of transcriptional responses across SSC concentrations, petal Venn analysis was performed on DEGs from the six comparison groups (276, 286, 296, 326, 376, and 426 mg/L vs. 0 mg/L) for gill and hepatopancreas tissues (Figure 10). The analysis revealed the number of treatments specific DEGs unique to each comparison group.

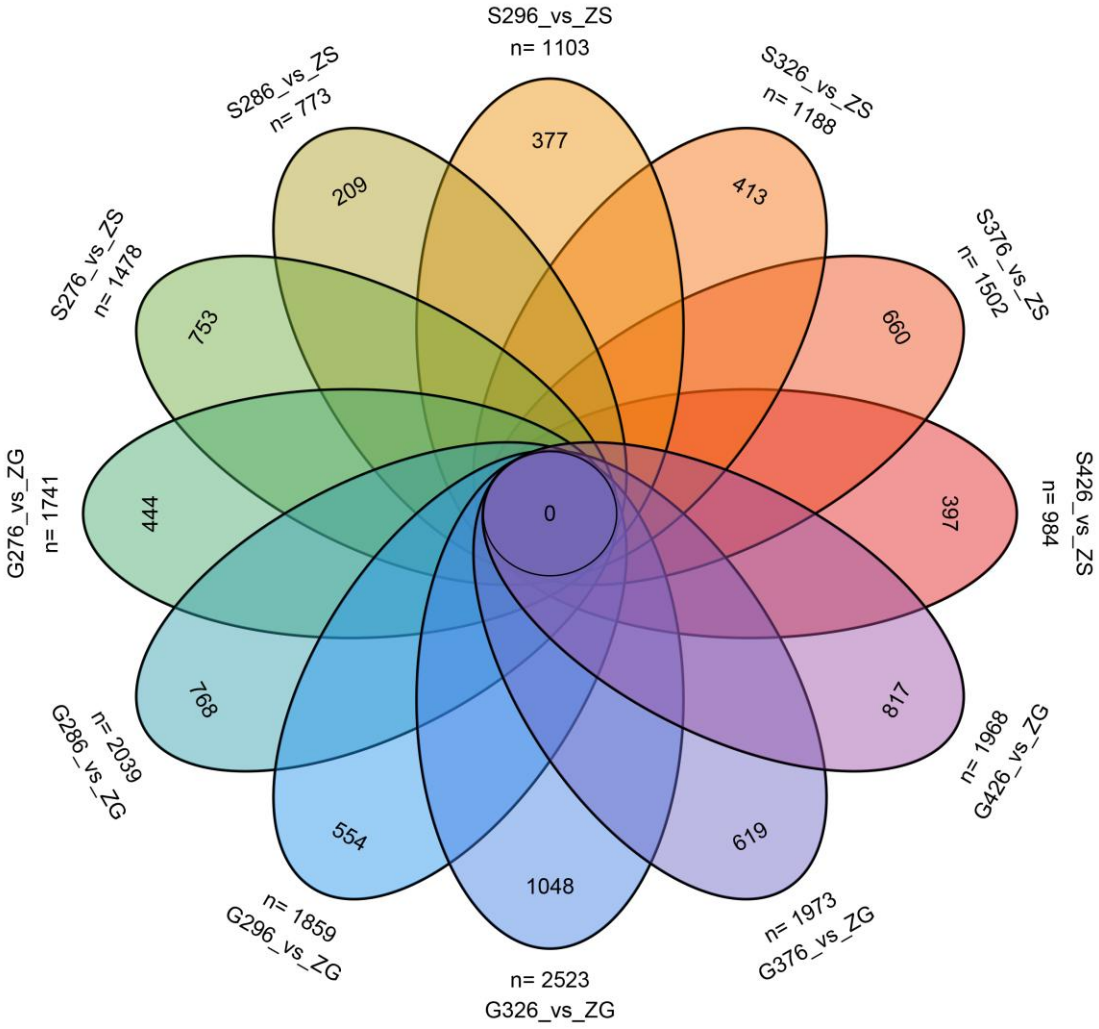


Figure 10. Venn diagrams showing DEG overlap among six SSC treatments (276, 286, 296, 326, 376, and 426 mg/L vs. 0 mg/L) in (A) gill and (B) hepatopancreas tissues. Each circle represents a treatment group, and numbers indicate DEG counts in each region. Sample labels: S, gill; G, hepatopancreas; numbers indicate SSC concentrations.

In the gill, the highest number of treatments specific DEGs was observed at 376 mg/L (660 genes), consistent with its high total DEG count, while the lowest number occurred at 286 mg/L (209 genes). In the hepatopancreas, the 326 mg/L treatment exhibited the highest number of unique DEGs (1048 genes), which corresponded to the maximum total DEG number detected in this tissue. Overall, the hepatopancreas produced more unique DEGs than the gill across most SSC gradients, demonstrating stronger tissue specific transcriptional reprogramming under SSC stress.

3.6 Differential Expression Gene Annotation

To elucidate the functional categories of the differentially expressed genes (DEGs) identified in each comparison, all DEGs were annotated against the Gene Ontology (GO) and Kyoto Encyclopedia of Genes and Genomes (KEGG) databases.

3.6.1 GO Annotation

GO annotation classified the DEGs into three major categories: biological process (BP), cellular component (CC), and molecular function (MF). Across all treatments and both tis-sues, BP terms consistently accounted for the largest proportion of annotated DEGs, followed by CC, while MF contributed the smallest fraction. The proportions of up regulated and down regulated DEGs varied across SSC treatments and between tissues.

In the hepatopancreas, dominant level 2 BP terms included cellular process, biological regulation, response to stimulus, and metabolic process, with additional contributions from multicellular organismal process, developmental process, localization, signaling, immune system process, and detoxification. Within the CC category, cellular anatomical entity and intracellular were most enriched, whereas protein containing complex and other organism related terms were less represented. For MF, binding and catalytic activity were overwhelmingly predominant, accompanied by transporter activity, molecular transducer activity, and transcription regulator activity. The total number of GO annotated DEGs fluctuated across the SSC gradient, consistent with the DEG count pattern shown in Section 3.7.

In the gill, DEGs were assigned to similar core GO term sets. BP terms were dominated by cellular process, biological regulation, metabolic process, and response to stimulus, with multicellular organismal process, developmental process, localization, signaling, and immune related processes also widely represented. CC and MF distributions were comparable to those in the hepatopancreas, with cellular

anatomical entity and intracellular predominating in CC, and binding and catalytic activity dominating MF. Notably, the balance between up and down regulated DEGs within individual GO terms differed between tissues, reflecting tissue specific functional responses to SSC stress.

3.6.2 KEGG Annotation

To investigate the metabolic and signaling pathways affected by SSC stress, all DEGs were annotated against the KEGG database. The number of KEGG annotated DEGs varied across treatments and tissues. In the hepatopancreas, annotated DEGs were primarily as-signed to five major KEGG categories: Metabolism, Genetic Information Processing, Environmental Information Processing, Cellular Processes, and Organismal Systems. Metabolism was the most abundantly represented category across all treatments, followed by Environmental Information Processing (Signal transduction) and Cellular Processes (Transport and catabolism, Cell growth and death). The highest number of KEGG annotated DEGs was observed at 426 mg/L (79 genes), while the lowest was at 286 mg/L (36 genes). Up regulated genes outnumbered down regulated genes in most hepato-pancreas treatments, except at 296 and 376 mg/L. Consistently represented pathways included Metabolic pathways (ko01100), Biosynthesis of secondary metabolites (ko01110), Microbial metabolism in diverse environments (ko01120), Carbon metabolism (ko01200), and Biosynthesis of amino acids (ko01230). Notably, the 426 mg/L treatment exhibited marked enrichment of Ribosome (ko03010) (54 up regulated genes), suggesting enhanced protein synthesis capacity under high SSC stress. Oxidative phosphorylation (ko00190), Thermogenesis (ko04714), and Cardiac muscle contraction (ko04260) were also prominently represented at 426 mg/L, indicating mitochondrial and metabolic activation, while Apoptosis (ko04210) and NOD like receptor signaling (ko04621) were annotated across multiple concentrations, suggesting involvement of programmed cell death and innate immune responses.

In the gill, KEGG annotated DEGs ranged from 2 (286 mg/L) to 24 (376 mg/L). Anno-tated pathways were more limited than in the hepatopancreas but consistently included Metabolic pathways (ko01100), Biosynthesis of secondary metabolites (ko01110), and Microbial metabolism in diverse environments (ko01120). MAPK signaling (ko04010), cAMP signaling (ko04024), and Calcium signaling (ko04020) were annotated at 326 and 376 mg/L, suggesting activation of stress related signal transduction cascades. Lysosome (ko04142) and Phagosome (ko04145) were also annotated across multiple concentrations, indicating lysosomal degradation and phagocytic activity in gill responses to SSC stress.

3.7 Functional Enrichment Analysis

3.7.1 GO Enrichment Analysis

Given that GO enrichment analysis involved 12 comparison groups (6 hepatopancreas + 6 gill), with each group containing enrichment results across the three GO categories (BP, CC, MF), all bubble plots were compiled into a multi panel figure (Figure 11, Figure 12) to ensure complete information presentation.

Across all comparison groups, the Biological Process (BP) category consistently showed the highest number of enriched GO terms, followed by Cellular Component (CC) and Molecular Function (MF).

Hepatopancreas

276 vs 0: 138 GO terms were enriched (FDR < 0.05). Enriched terms included extra-cellular space, extracellular region, protein trimerization, chemical homeostasis, positive regulation of cytokine production, positive regulation of protein transport, activation of innate immune response, iron ion homeostasis, Notch signaling pathway, carbohydrate binding, and identical protein binding (Figure 11A).

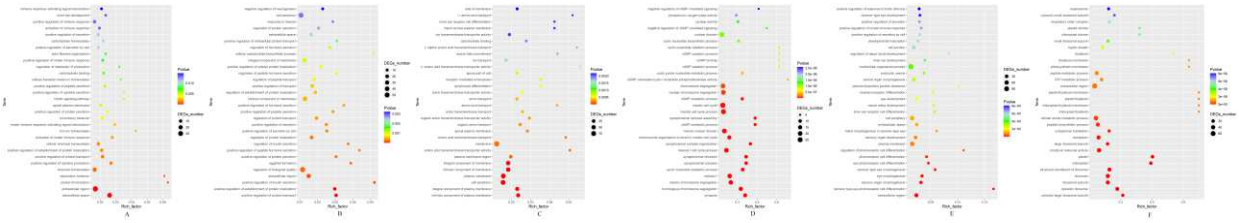


Figure 11. GO enrichment bubble plots of DEGs in hepatopancreas and gill tissues across all SSC treatments versus the 0 mg/L control. (A) Hepatopancreas, 276 vs 0; (B) Hepatopancreas, 286 vs 0; (C) Hepatopancreas, 296 vs 0; (D) Hepatopancreas, 326 vs 0; (E) Hepatopancreas, 376 vs 0; (F) Hepatopancreas, 426 vs 0. The x axis represents the enrichment factor (ratio_in_study / ra-tio_in_pop), the y axis indicates GO terms, and the size and colour of each bubble represent the number of DEGs and the FDR adjusted p value, respectively. Only GO terms with FDR < 0.05 are shown.

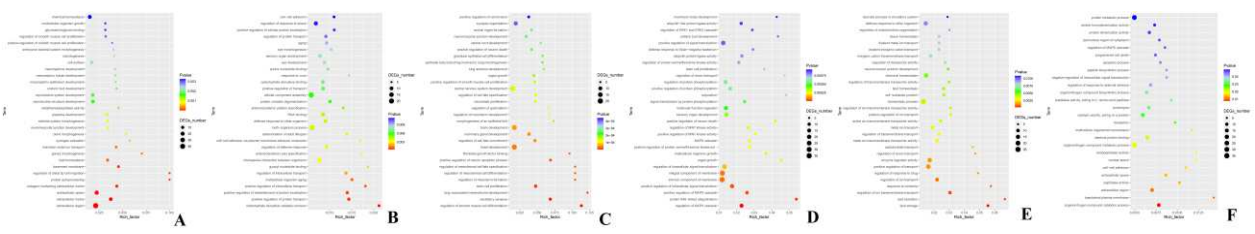


Figure 12. GO enrichment bubble plots of DEGs in hepatopancreas and gill tissues across all SSC treatments versus the 0 mg/L control. (A) Gill, 276 vs 0; (B) Gill, 286 vs 0; (C) Gill, 296 vs 0; (D) Gill, 326 vs 0; (E) Gill, 376 vs 0; (F) Gill, 426 vs 0. The x axis represents the enrichment factor (ratio_in_study / ratio_in_pop), the y axis indicates GO terms, and the size and colour of each bubble represent the number of DEGs and the FDR adjusted p value, respectively. Only GO terms with FDR < 0.05 are shown.

286 vs 0: 138 GO terms were enriched (FDR < 0.05). Enriched terms included positive regulation of protein transport, extracellular region, regulation of biological quality, positive regulation of protein secretion, intrinsic component of membrane, response to hexose, plasma membrane, response to stress, and cell periphery (Figure 11B).

296 vs 0: 166 GO terms were enriched (FDR < 0.05). Enriched terms included intrinsic component of plasma membrane, integral component of plasma membrane, cell periphery, plasma membrane, amino acid transmembrane transporter activity, organic anion transport, anion transmembrane transport, lymphocyte differentiation, receptor mediated endocytosis, and ion transport (Figure 11C).

326 vs 0: 256 GO terms were enriched (FDR < 0.05). Enriched terms included synapsis, homologous chromosome segregation, meiotic chromosome segregation, meiosis I, cyclic nucleotide metabolic process, synaptonemal complex, cAMP metabolic process, cGMP metabolic process, nuclear chromosome segregation, cell cycle, and chromosome segregation (Figure 11D).

376 vs 0: 192 GO terms were enriched (FDR < 0.05). Enriched terms included extra-cellular region, photoreceptor cell differentiation, sensory organ morphogenesis, eye morphogenesis, plasma membrane, respiratory chain complex, innate immune response, cell death, programmed cell death, cell junction, and response to hypoxia (Figure 11E).

426 vs 0: 306 GO terms were enriched (FDR < 0.05). Enriched terms included structural constituent of ribosome, cytosolic large ribosomal subunit, ribosomal subunit, cytosolic ribosome, ribosome, translation, cytoplasmic translation, peptide biosynthetic process, structural molecule activity, ATP metabolic process, extracellular region, ion trans-membrane transport, respiratory chain complex, and antimicrobial humoral immune response (Figure 11F).

Gill

276 vs 0: 133 GO terms were enriched (FDR < 0.05). Enriched terms included extra-cellular region, extracellular matrix, extracellular space, collagen containing extracellular matrix, lipid homeostasis, transition metal ion transport, G protein coupled receptor signaling pathway, cell surface, and skeletal system morphogenesis (Figure 12A).

286 vs 0: 63 GO terms were enriched (FDR < 0.05). Enriched terms included carbohydrate derivative catabolic process, positive regulation of protein transport, multicellular organism aging, guanyl nucleotide binding, cell adhesion, RNA binding, defense response to other organism, eye development, and sensory organ development (Figure 12B).

296 vs 0: 109 GO terms were enriched (FDR < 0.05). Enriched terms included regulation of smooth muscle cell differentiation, excitatory synapse, stem cell proliferation, brain development, neuroblast proliferation, central nervous system development, synapse organization, neuromuscular junction development, cell junction organization, growth fac-tor binding, calcium ion binding, and ATPase activity (Figure 12C).

326 vs 0: 113 GO terms were enriched (FDR < 0.05). Enriched terms included regulation of MAPK cascade, positive regulation of MAPK cascade, protein K48 linked ubiquitination, positive regulation of intracellular signal transduction, intrinsic component of membrane, integral component of membrane, organ growth, multicellular organism growth, positive regulation of protein serine/threonine kinase activity, MAPK cascade, sensory organ development, and Golgi apparatus (Figure 12D).

376 vs 0: 138 GO terms were enriched (FDR < 0.05). Enriched terms included lipid storage, acid secretion, regulation of ion transmembrane transport, response to ischemia, positive regulation of transport, enzyme regulator activity, metal ion transmembrane transporter activity, homeostatic process, lipid homeostasis, apoptotic process, and defense response to another organism (Figure 12E).

426 vs 0: 68 GO terms were enriched (FDR < 0.05). Enriched terms included organonitrogen compound catabolic process, basolateral plasma membrane, extracellular region, extracellular space, peptidase activity cell adhesion, nuclear speck, endopeptidase activity, translation, peptide biosynthetic process, apoptotic process, and protein homodimerization activity (Figure 12F).

3.7.2 KEGG Enrichment Analysis

To identify the biological pathways significantly affected by SSC stress, KEGG enrichment analysis was performed on DEGs from each comparison group. All bubble plots were compiled into a multi panel figure (Figure 13, Figure 14).

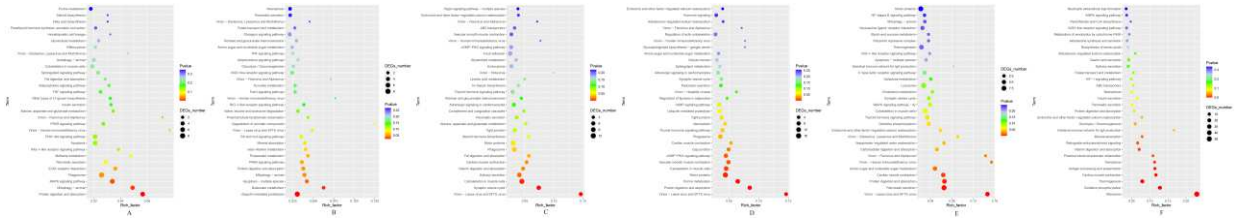


Figure 13. KEGG enrichment bubble plots of DEGs in gill and hepatopancreas tissues across all SSC treatments versus the 0 mg/L control. (A) Hepatopancreas, 276 vs 0; (B) Hepatopancreas, 286 vs 0; (C) Hepatopancreas, 296 vs 0; (D) Hepatopancreas, 326 vs 0; (E) Hepatopancreas, 376 vs 0; (F) Hepatopancreas, 426 vs 0. The x axis represents the enrichment factor, the y axis indicates KEGG pathways, and the size and colour of each bubble represent the number of DEGs and the FDR adjusted p value, respectively. Only pathways with FDR < 0.05 are shown.

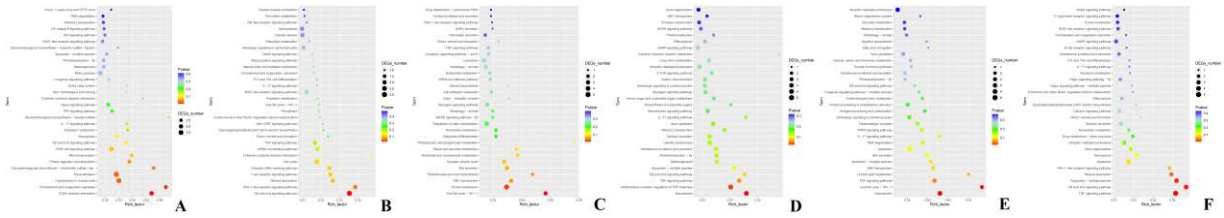


Figure 14. KEGG enrichment bubble plots of DEGs in gill and hepatopancreas tissues across all SSC treatments versus the 0 mg/L control. (A) Gill, 276 vs 0; (B) Gill, 286 vs 0; (C) Gill, 296 vs 0; (D) Gill, 326 vs 0; (E) Gill, 376 vs 0; (F) Gill, 426 vs 0. The x axis represents the enrichment factor, the y axis indicates KEGG pathways, and the size and colour of each bubble represent the number of DEGs and the FDR adjusted p value, respectively. Only pathways with FDR < 0.05 are shown.

Hepatopancreas

276 vs 0: Enriched pathways included Fatty acid biosynthesis, Fatty acid degradation, Sphingolipid metabolism, Lysosome, Phagosome, Apoptosis, Mitophagy, Autophagy, MAPK signaling, cAMP signaling, TNF signaling, and NOD like receptor signaling (Figure 13A).

286 vs 0: Enriched pathways included Glycolysis / Gluconeogenesis, Citrate cycle (TCA cycle), Pyruvate

metabolism, Fatty acid degradation, Oxidative phosphorylation, Ribosome, Spliceosome, Ubiquitin mediated proteolysis, Apoptosis, Necroptosis, Ferroptosis, MAPK signaling, NF kappa B signaling, Calcium signaling, and NOD like receptor signaling (Figure 13B).

296 vs 0: Enriched pathways included Arachidonic acid metabolism, Fatty acid degradation, Steroid hormone biosynthesis, N glycan biosynthesis, Sphingolipid metabolism, Lysosome, Phagosome, Endocytosis, Apoptosis, Autophagy, PI3K Akt signaling, mTOR signaling, and TNF signaling (Figure 13C).

326 vs 0: Enriched pathways included Purine metabolism, Pyrimidine metabolism, Glutathione metabolism, Glycolysis / Gluconeogenesis, Ribosome, Spliceosome, DNA replication, Ubiquitin mediated proteolysis, Apoptosis, Necroptosis, Ferroptosis, MAPK signaling, cGMP PKG signaling, cAMP signaling, Calcium signaling, PI3K Akt signaling, mTOR signaling, FoxO signaling, Phagosome, Lysosome, and Thermogenesis (Figure 13D).

376 vs 0: Enriched pathways included Oxidative phosphorylation, Fatty acid bio-synthesis, Fatty acid degradation, Sphingolipid metabolism, Ribosome, Spliceosome, Ubiquitin mediated proteolysis, Apoptosis, Necroptosis, Lysosome, Phagosome, MAPK signaling, NF kappa B signaling, TNF signaling, NOD like receptor signaling, Toll and Imd signaling, and IL 17 signaling (Figure 13E).

426 vs 0: Enriched pathways included Glycolysis / Gluconeogenesis, Pyruvate metabolism, Oxidative phosphorylation, Citrate cycle (TCA cycle), Fatty acid degradation, Arachidonic acid metabolism, Glutathione metabolism, Purine metabolism, Pyrimidine metabolism, Ribosome, Spliceosome, Ubiquitin mediated proteolysis, Apoptosis, Necroptosis, Ferroptosis, Lysosome, Phagosome, Endocytosis, MAPK signaling, cAMP signaling, cGMP PKG signaling, Calcium signaling, Ras signaling, Rap1 signaling, PI3K Akt signaling, AMPK signaling, mTOR signaling, TNF signaling, NF kappa B signaling, NOD like receptor signaling, Toll and Imd signaling, IL 17 signaling, and Thermogenesis (Figure 13F).

Gill

276 vs 0: Enriched pathways included Purine metabolism, Glycosaminoglycan bio-synthesis, Sphingolipid metabolism, Lysosome, Apoptosis, PI3K Akt signaling, MAPK signaling, cAMP signaling, Calcium signaling, Phagosome, and ECM receptor interaction (Figure 14A).

286 vs 0: Enriched pathways included Glycolysis / Gluconeogenesis, Oxidative phosphorylation, Purine metabolism, Pyrimidine metabolism, Ribosome, Spliceosome, Cell cycle, Oocyte meiosis, PI3K Akt signaling, Apoptosis, and NOD like receptor signaling (Figure 14B).

296 vs 0: Enriched pathways included Arachidonic acid metabolism, Steroid biosynthesis, Glycerolipid metabolism, Ribosome, Lysosome, Phagosome, Apoptosis, PI3K Akt signaling, TNF signaling, and FoxO signaling (Figure 14C).

326 vs 0: Enriched pathways included Glutathione metabolism, Sphingolipid metabolism, Ribosome, Spliceosome, Ubiquitin mediated proteolysis, Apoptosis, MAPK signaling, Rap1 signaling, Calcium signaling, cGMP PKG signaling, cAMP signaling, PI3K Akt signaling, Phagosome, and Lysosome (Figure 14D).

376 vs 0: Enriched pathways included Carbon metabolism, Biosynthesis of amino acids, Fatty acid metabolism, Starch and sucrose metabolism, Ribosome, Spliceosome, RNA degradation, mRNA surveillance pathway, Apoptosis, MAPK signaling, Rap1 signaling, Calcium signaling, cAMP signaling, PI3K Akt signaling, and PPAR signaling (Figure 14E).

426 vs 0: Enriched pathways included Arachidonic acid metabolism, Glutathione metabolism, Ribosome, Spliceosome, Lysosome, Apoptosis, NOD like receptor signaling, TNF signaling, MAPK signaling, Hippo signaling, and Neurotrophin signaling (Figure 14F).

3.8 Quantitative Real Time PCR (qRT-PCR) Validation

To validate the reliability of the RNA seq data, twelve differentially expressed genes (DEGs) were selected for qRT-PCR analysis based on their expression patterns in the 426 mg/L treatment compared to the 0 mg/L control. The selected genes covered multiple functional categories, including energy metabolism, ion transport, cytoskeletal organisation, and stress responses. 18S rRNA was used as the internal reference gene, and the $2^{-}\Delta\Delta Ct$ method was employed to calculate relative expression levels.

The qRT-PCR results showed that the overall expression trends of most selected genes were consistent with the RNA seq data (Table 4). Among the twelve genes, DN44109 (collagen alpha 1(X) chain like) and DN94928 (cytochrome c oxidase subunit III) exhibited significant up regulation in the 426 mg/L treatment, with qPCR relative expression levels of 3.87± 0.32 and 5.79 ± 0.57, respectively, consistent

with their RNA seq log_2FC values (4.77 and 7.42). DN88965 (catenin alpha-2-like) showed significant down-regulation, with a qPCR value of 0.28 ± 0.05, corroborating its negative log_2FC value (−2.37). Several other genes (DN37274, DN48737, DN55951, DN95997) showed moderate expression changes consistent with RNA-seq trends, though the magnitudes differed between the two plat-forms. Three genes (DN37274, DN41008, and DN57710) showed discordant trends be-tween the two platforms, which may reflect technical differences in primer efficiency, transcript isoform specificity, or biological variability between individual samples. Notably, DN57710 (glutathione S-transferase theta-1-like) showed a discordant trend, with RNA-seq log_2FC = −10.34 but qPCR = 1.71 ± 0.18. Nevertheless, the overall qRT-PCR vali-dation supported the reliability of the transcriptomic data for most selected genes, while highlighting the importance of considering platform-specific differences. To compare the two platforms on a comparable scale, RNA-seq log_2 fold changes were compared with log_2-transformed qRT-PCR relative expression values. For all 12 genes, the Pearson correlation coefficient was r = 0.333 (p = 0.290, n = 12). When the three discordant genes (DN37274, DN41008, and DN57710) were excluded, the correlation increased to r = 0.700 (p = 0.036, n = 9), indicating significant and moderate-to-strong consistency for the remaining genes. These results are summarized in Supplementary Table S3.

Table 4. Comparison of RNA-seq and qRT-PCR expression changes for selected DEGs in the 426 mg/L treatment.

Gene ID	Putative Function	RNA-seq log_2FC	qRT-PCR ($2^{-}\Delta\Delta$Ct)	Trend Consistency
TRINITY_DN145_c0_g1	ATP synthase subunit beta	10.29	2.72 ± 0.59	Concordant (up)
TRINITY_DN37274_c0_g1	Sodium channel protein	–9.54	2.40 ± 0.30	Discordant
TRINITY_DN37408_c0_g1	NADH dehydrogenase subunit 1	6.70	3.34 ± 0.56	Concordant (up)
TRINITY_DN41008_c0_g1	Regulator of G-protein signalling 17-like	8.80	0.97 ± 0.15	Discordant

Gene ID	Putative Function	RNA-seq $\log_2$FC	qRT-PCR ($2^{-}\Delta\Delta$Ct)	Trend Consistency
TRINITY_DN44109_c0_g1	Collagen alpha-1(X) chain-like	4.77	3.87 ± 0.32	Concordant (up)
TRINITY_DN48737_c0_g1	Tubulin beta-1/beta-2 chain	6.62	1.60 ± 0.24	Concordant (up)
TRINITY_DN55951_c0_g1	Mucin-21-like	13.43	2.80 ± 0.34	Concordant (up)
TRINITY_DN57710_c0_g1	Glutathione S-transferase theta-1-like	–10.34	1.71 ± 0.18	Discordant
TRINITY_DN6215_c0_g1	Na^+/K^+-transporting ATPase subunit beta-1	10.37	2.57 ± 0.48	Concordant (up)
TRINITY_DN88965_c0_g1	Catenin alpha-2-like	–2.37	0.28 ± 0.05	Concordant (down)
TRINITY_DN94928_c0_g1	Cytochrome c oxidase subunit III	7.42	5.79 ± 0.57	Concordant (up)
TRINITY_DN95997_c0_g1	Carbonic anhydrase 4 precursor	10.32	3.00 ± 0.69	Concordant (up)

Note: Values are presented as mean ± SD (n = 3). "Concordant" indicates that the direction of expression change (up-regulated, down-regulated, or no change) was consistent between RNA-seq and qRT-PCR; "Discordant" indicates opposite directions between the two methods.

4. Discussion

In this study, we conducted a combined transcriptomic and ultrastructural investigation to elucidate the molecular and cellular responses of the hard clam *M. meretrix* to suspended sediment stress. Tissue-specific transcriptional reprogramming was observed, with the hepatopancreas exhibiting substantially more pronounced and diverse responses than the gill. TEM analysis further revealed a clear dose-dependent progression of ultra-structural damage in gill epithelial cells, ranging from early reversible stress to terminal necrosis. These findings provide multi-tissue evidence that *M. meretrix* employs

distinct molecular and structural strategies in different tissues under particle-rich environ-ments.4.1 Differential Transcriptional Responses Between the Gill and Hepatopancreas

One of the most prominent findings of this study was the marked difference in transcriptional responsiveness between the gill and hepatopancreas. The hepatopancreas consistently exhibited 1.5- to 2-fold higher numbers of DEGs compared to the gill across all SSC concentrations, with peak values of 2,567 DEGs in the hepatopancreas (326 mg/L) versus 1,549 in the gill (376 mg/L). This tissue-specific disparity aligns with observations in other bivalves exposed to environmental stressors [36-38]. For instance, in the razor clam Sinonovacula constricta under combined ammonia and hypoxia stress, the hepatopancreas and gill exhibited distinct transcriptional profiles reflecting their specialised functions [36]. Similarly, in the shrimp Macrobrachium nipponense under salinity acclimation, the hepatopancreas showed stronger metabolic reprogramming, whereas the gill was more enriched in ion transport and barrier-related genes [37]. In Litopenaeus vannamei under alkalinity stress, the hepatopancreas also displayed a more pronounced immune and detoxification response than the gill [38].

The functional divergence between these two tissues is rooted in their distinct physiological roles. The gill serves as the primary interface between the organism and its external environment, responsible for particle capture, gas exchange, and initial immune surveillance. Its relatively moderate transcriptional response—characterised by up-regulation of genes involved in ECM-receptor interaction, cell adhesion molecules, tight junctions, gap junctions, and actin cytoskeleton regulation—suggests a strategy focused on structural reinforcement and barrier maintenance. This is consistent with the role of the gill as a physical barrier that must withstand direct mechanical abrasion from suspended particles. The enrichment of lysosome and phagosome pathways in the gill further supports its role in particle clearance and innate immune defence at the entry site.

In contrast, the hepatopancreas, as the primary metabolic and detoxification organ in bivalves, exhibited a far more extensive and diverse transcriptional response. The prominent enrichment of metabolism-related pathways—including glycolysis/gluconeogenesis, citrate cycle (TCA cycle), oxidative phosphorylation, and fatty acid metabolism—indicates substantial metabolic reprogramming to meet the energetic demands of stress response and tissue repair. The hepatopancreas also showed strong enrichment of immune-related pathways such as NOD-like receptor signaling, TNF signaling, NF-κB signaling, and Toll and Imd signaling, suggesting that this tissue plays a central role in systemic immune

surveillance and inflammatory responses to particle-associated stress.

These differential response patterns between tissues are consistent with the concept that different organs may adopt distinct transcriptional strategies to cope with environ-mental stress. The gill prioritises immediate physical defence and particle clearance, while the hepatopancreas orchestrates a more complex response involving metabolic adaptation, detoxification, and immune activation. This functional specialisation likely reflects the evolutionary adaptation of bivalves to their filter-feeding lifestyle, where the gill must continuously manage particle influx while the hepatopancreas processes absorbed materials and mounts systemic responses.

Our results extend these findings to SSC stress in *M. meretrix*, showing that the hepatopancreas consistently mounted a broader transcriptional response than the gill across all SSC concentrations.

4.2 Ultrastructural Damage and Its Association with Transcriptomic Responses

TEM analysis provided direct cellular-level evidence for the dose-dependent toxicity of SSC stress in the gill of *M. meretrix*. At 276 mg/L, the ultrastructural changes were relatively mild and mainly included local chromatin margination, mild mitochondrial swelling, increased cytoplasmic vesicles, and ciliary disorganization, suggesting an early and potentially reversible stress response. As SSC increased to 286–326 mg/L, the damage progressed to moderate and severe stages, characterized by extensive ciliary shedding, chromatin aggregation and margination, mitochondrial swelling and cristae dissolution, endoplasmic reticulum dilation, cytoplasmic vacuolization, and loosening of intercellular junctions. At the highest concentrations (376 and 426 mg/L), the gill epithelium exhibited near-terminal to terminal necrotic damage, including nuclear pyknosis, nuclear membrane rupture, karyolysis, complete organelle disintegration, abundant myelin figures, and col-lapse of the epithelial barrier.

These ultrastructural alterations were highly consistent with the transcriptomic responses observed in this study. The enrichment of oxidative phosphorylation, TCA cycle, and glycolysis/gluconeogenesis pathways may reflect an attempt to meet the increased energy demand caused by particle stress, while the extensive mitochondrial swelling and cristae dissolution observed by TEM suggest that this compensatory response ultimately fails under high SSC exposure. Similarly, the enrichment of ECM–receptor interaction, cell adhesion, tight junction, and actin cytoskeleton-related genes in the gill is consistent with the TEM findings of ciliary disorganization, widened intercellular spaces, and disrupted

cell junctions. The enrichment of apoptosis, necroptosis, and ferroptosis pathways corresponds well with the observed nuclear condensation, nuclear membrane rupture, organelle disintegration, and myelin figure formation, which are typical features of programmed cell death and necrosis.

The enrichment of glutathione metabolism and oxidative stress-related pathways further supports the idea that SSC stress induces oxidative damage, which may contribute to membrane lipid peroxidation, mitochondrial dysfunction, and eventual cell death. In addition, the activation of NOD-like receptor, TNF, NF-κB, and Toll and Imd signaling pathways suggests that the damaged cells and released debris may trigger innate immune and inflammatory responses in the gill. Taken together, the TEM and transcriptomic results indicate that SSC stress causes a dose-dependent progression from early cellular stress to irreversible necrosis and epithelial barrier failure in the gill. However, because TEM analysis in this study focused on the gill, the ultrastructural basis of the stronger hepatopancreatic transcriptomic response remains to be investigated in future studies.4.3 Concentration-Dependent Transcriptional Patterns and the Decline at 426 mg/L

The number of DEGs exhibited a non-monotonic, concentration-dependent pattern in both tissues. In the gill, DEG counts fluctuated from 1,494 at 276 mg/L down to 791 at 286 mg/L, then progressively increased to 1,549 at 376 mg/L, before declining to 1,004 at 426 mg/L. In the hepatopancreas, DEG counts increased from 1,775 at 276 mg/L to a peak of 2,567 at 326 mg/L, then decreased to 2,002 and 2,003 at 376 and 426 mg/L, respectively.

The decline in DEG numbers at the highest SSC concentration (426 mg/L) is particularly intriguing. Several non-mutually exclusive explanations may account for this phenomenon. One possible explanation is that adaptive transcriptional reprogramming occurs under extreme stress. We hypothesise that, at very high SSC concentrations, clams may shift from an active stress-response strategy to a more energy-conserving “survival mode,” in which transcriptional activity is down-regulated to reduce energetic costs. However, this remains a hypothesis that requires functional validation. A second, albeit speculative, possibility is that the 426 mg/L treatment represents a concentration beyond which the transcriptional machinery becomes compromised, either through physical damage to cellular components or through exhaustion of transcriptional resources. The fact that substantial numbers of DEGs were still detected at 426 mg/L (1,004 in gill and 2,003 in hepatopancreas) argues against complete transcriptional shutdown, but partial suppression cannot be ruled out. These interpretations should be regarded as

hypotheses, and future functional studies are needed to distinguish among them.

This non linear concentration response pattern has implications for environmental risk assessment. It suggests that the relationship between SSC concentration and biological effect is not simply monotonic, and that moderate concentrations (296–376 mg/L) may elicit stronger molecular responses than the highest concentrations. Similar non-monotonic responses have been reported for suspended sediment exposure across aquatic taxa. A systematic review by Park et al. [39] noted that biological responses to suspended sediments often do not follow a simple linear dose–response relationship. In particular, a multibiomarker study on Manila clams exposed to dredged sediments demonstrated that the hepatopancreas is the most sensitive tissue for detecting sublethal stress responses, consistent with our observation that the hepatopancreas exhibited more pronounced transcriptional changes than the gill [40].

4.4 Key Pathways and Molecular Mechanisms

4.4.1 Energy Metabolism and Mitochondrial Function

A hallmark of the SSC-induced transcriptional response was the robust enrichment of energy metabolism pathways, particularly in the hepatopancreas at higher concentrations. Oxidative phosphorylation (ko00190) and the citrate cycle (TCA cycle) (ko00020) were consistently enriched at 376 and 426 mg/L, while glycolysis/gluconeogenesis (ko00010) and pyruvate metabolism (ko00620) were prominent across multiple concentrations. This widespread enrichment of genes in energy metabolism pathways may suggest that SSC stress imposes substantial energetic demands on clams [41], although metabolic rates were not directly measured. This is consistent with the transcriptional response of Lembulus bi-cuspidatus to hypoxia–reoxygenation, in which key metabolic genes were also affected [41].

The up-regulation of oxidative phosphorylation genes, including multiple subunits of cytochrome c oxidase (e.g., DN94928, validated by qPCR) and NADH dehydrogenase (e.g., DN37408), may suggest increased mitochondrial activity to meet ATP demands for detoxification, tissue repair, and immune function [42]. This is consistent with observations in Crassostrea gigas under hypoxia, where mitochondrial electron transport chain genes were also induced [42].

The marked enrichment of thermogenesis (ko04714) and cardiac muscle contraction (ko04260) pathways at 426 mg/L in the hepatopancreas is notable. In mammals, thermo-genesis is primarily associated with heat production via mitochondrial uncoupling; how-ever, in non mammalian organisms, enrichment of

this pathway may reflect broad metabolic perturbations rather than classical thermogenesis. The concurrent enrichment of oxidative phosphorylation and thermogenesis pathways at the highest SSC concentration may thus indicate stress induced alterations in mitochondrial energy metabolism, potentially including inefficient ATP production or enhanced electron transport chain activity to meet elevated energetic demands while managing reactive oxygen species (ROS) pro-duction.

4.4.2 Ribosome Biogenesis and Protein Synthesis

The most striking pathway enrichment at 426 mg/L in the hepatopancreas was ribosome (ko03010), with 54 up-regulated genes. This marked up-regulation of ribosomal protein may suggest enhanced protein synthesis capacity under extreme SSC stress, although translational activity was not directly measured. This finding is consistent with the in-creased energetic demands discussed above: to sustain the production of stress-response proteins (e.g., heat shock proteins, antioxidant enzymes, immune effectors), clams must increase their translational capacity.

The qPCR validation of multiple ribosomal and mitochondrial genes (e.g., DN145 encoding ATP synthase subunit beta, DN37408 encoding NADH dehydrogenase subunit 1) confirmed the reliability of these transcriptomic observations. The near-complete sup-pression of DN88965 (catenin alpha-2-like) at 426 mg/L (0.008-fold by qPCR) is particularly noteworthy, as catenins are critical for cell-cell adhesion and cytoskeletal integrity. Its dramatic down-regulation may indicate disruption of adherens junctions and epithelial barrier function under extreme SSC stress. Although ribosomal biogenesis has been less frequently reported in bivalve stress studies, the up-regulation of ribosomal protein genes under stress has been observed in other marine invertebrates, suggesting a conserved translational response to environmental challenge.

4.4.3 Cell Death Pathways: Apoptosis, Necroptosis, and Ferroptosis

The consistent enrichment of cell death pathways across multiple SSC concentrations and both tissues suggests cytotoxic effects of suspended sediment exposure [43]. This is consistent with observations in Chlamys nobilis under low-temperature stress, where caspase genes showed altered expression [43]. Apoptosis (ko04210) was enriched in both gill and hepatopancreas across most comparisons, while necroptosis (ko04217) and ferroptosis (ko04216) were also prominently represented, particularly at higher concentrations.

The simultaneous enrichment of genes in multiple cell death pathways may suggest that SSC stress triggers diverse forms of programmed cell death depending on the severity and duration of exposure [44]. In Mytilus edulis and Crassostrea gigas exposed to inter-mittent hypoxia, cell survival and inflammatory pathways were also affected [44]. How-ever, functional validation is needed to confirm whether these pathways are activated in *M. meretrix*. Apoptosis, as a regulated and non-inflammatory form of cell death, may rep-resent a controlled mechanism for removing damaged cells without eliciting excessive in-flammation. Necroptosis, in contrast, is a more inflammatory form of cell death that may contribute to tissue damage and immune activation. Ferroptosis, an iron-dependent form of cell death driven by lipid peroxidation, is consistent with the observed enrichment of glutathione metabolism and oxidative stress pathways.

The presence of these cell death pathways in both tissues, but with greater representation in the hepatopancreas, suggests that the hepatopancreas may be more susceptible to particle-induced cytotoxicity, possibly due to its role in metabolising and detoxifying ab-sorbed materials. This tissue-specific vulnerability may contribute to the stronger cytotoxic response observed in the hepatopancreas.

4.4.4 Immune and Inflammatory Responses

Immune-related pathways were prominently enriched across both tissues, with a clear concentration-dependent pattern. NOD-like receptor signaling (ko04621), TNF signaling (ko04668), NF-κB signaling (ko04064), Toll and Imd signaling (ko04624), and IL-17 signaling (ko04657) were consistently enriched in the hepatopancreas at moderate to high concentrations [45]. This is consistent with the immune response observed in Ruditapes philippinarum challenged with lipopolysaccharide, where NOD-like receptor and TNF signaling pathways were also enriched [45]. The gill showed enrichment of these path-ways primarily at higher concentrations (376 and 426 mg/L).

The enrichment of genes in these innate immune pathways may indicate that SSC stress is perceived as a “danger signal” by clams, potentially triggering inflammatory responses analogous to those seen during pathogen infection. This interpretation remains hypothetical and requires functional validation. This is consistent with the concept that physical particles can activate pattern recognition receptors (PRRs) either directly through particle-associated molecular patterns or indirectly through damage-associated molecular patterns (DAMPs) released from damaged cells.

The NOD-like receptor (NLR) signaling pathway is particularly relevant, as NLRs are cytosolic sensors that detect both microbial components and cellular damage, leading to the activation of inflammatory responses and pyroptosis [46]. In Mytilus coruscus under rising seawater temperature, immune-related pathways including TNF and NLR signaling were also enriched [46]. The enrichment of this pathway across multiple concentrations may suggest that SSC stress induces cellular damage that is sensed by NLRs, potentially triggering inflammatory cascades; however, direct evidence of NLR activation is lacking.

The TNF signaling pathway mediates diverse cellular responses including inflammation, apoptosis, and cell survival. Its enrichment in both tissues may suggest the involvement of TNF-mediated signalling in the SSC stress response, which could contribute to both protective and detrimental outcomes. However, direct evidence of pathway activation is lacking.

The involvement of the Toll and Imd signaling pathway (the invertebrate equivalent of mammalian Toll-like receptor pathways) may support the involvement of innate immune responses; however, functional activation was not directly tested. In bivalves, Toll-like receptors recognise a wide range of pathogen-associated and damage-associated molecular patterns, making them central to both anti-microbial defence and stress responses.

4.4.5 Oxidative Stress and Detoxification

The enrichment of glutathione metabolism (ko00480) suggests that SSC stress induces oxidative stress and activates detoxification pathways [47]. However, individual glutathione S-transferase genes can show divergent responses, and pathway enrichment alone does not establish functional activation. For example, DN57710 exhibited a discordant trend between RNA-seq ($log_2FC = -10.34$) and qRT-PCR (1.71 ± 0.18), highlighting the im-portance of interpreting pathway-level enrichment with caution and validating individual genes by multiple methods. Glutathione is a critical antioxidant that protects cells against ROS and facilitates the detoxification of xenobiotics. The up-regulation of glutathione metabolism genes suggests that clams are actively combating oxidative stress generated by particle exposure.

The induction of glutathione S-transferase (GST) is particularly significant, as GSTs catalyse the conjugation of glutathione to electrophilic substrates, facilitating their excretion. The up-regulation of

GST genes in response to SSC stress suggests that suspended particles may either directly introduce pro-oxidant compounds or indirectly generate ROS through cellular damage and inflammatory responses. This is consistent with studies showing that suspended sediment can exacerbate the toxicity of other contaminants through ROS generation [39].

A schematic summary integrating the observed and proposed responses of the gill and hepatopancreas to SSC stress is presented in Figure 15.

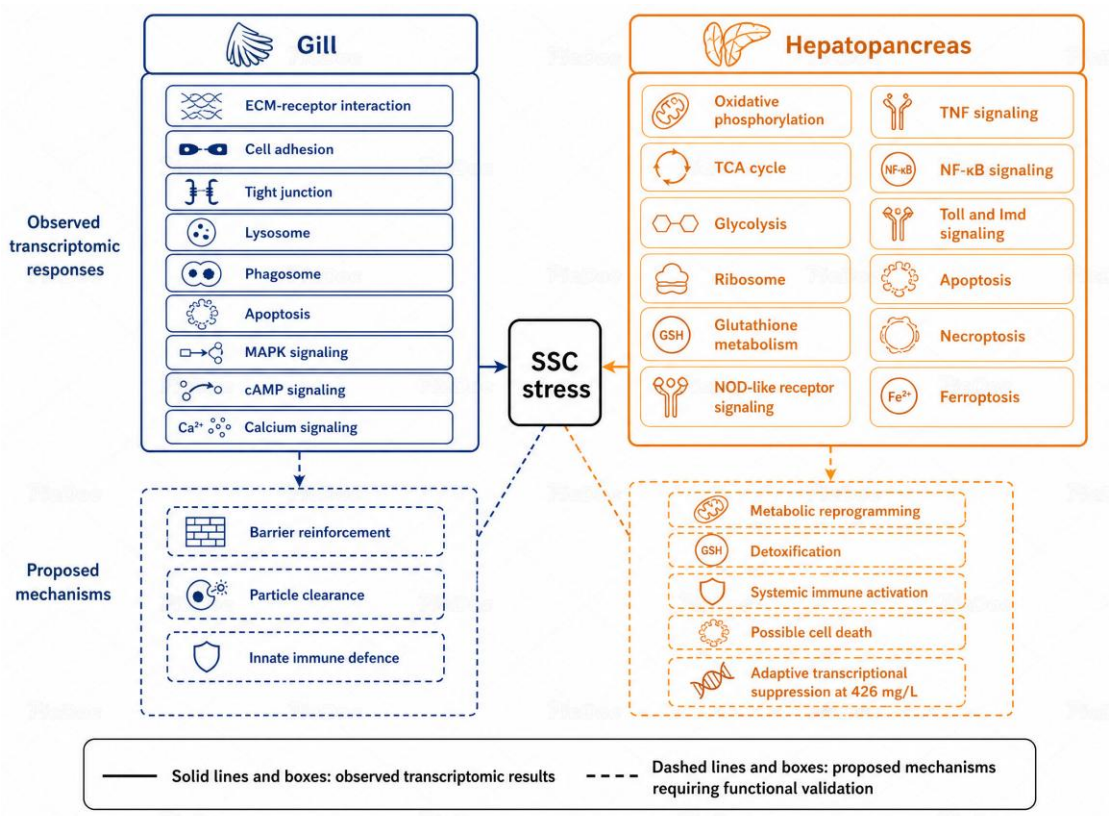


Figure 15. Schematic summary of the observed and proposed responses of the gill and hepato-pancreas of *M. meretrix* to suspended sediment stress (SSC). The central box represents SSC stress. The left and right columns represent the gill and hepatopancreas, respectively. The upper panels (solid lines and boxes) summarise the observed transcriptomic responses based on differentially expressed genes and functional enrichment analyses, including energy metabolism, oxidative stress defence, innate immune signalling, and cell death pathways. The lower panels (dashed lines and boxes) indicate proposed mechanisms that are inferred from the transcriptomic data but remain hypothetical and require functional validation. The legend at the bottom clarifies that solid lines and boxes denote observed results, whereas dashed lines and boxes denote proposed mechanisms. Key proposed mechanisms include barrier reinforcement, particle clearance, and innate immune defence in the gill, and metabolic reprogramming,

detoxification, systemic immune activation, possible cell death, and adaptive transcriptional suppression at 426 mg/L in the hepato-pancreas. The proposed mechanisms should be regarded as hypotheses rather than established conclusions.

4.5 Environmental Implications and Study Limitations

The findings of this study have important implications for environmental risk assessment in coastal engineering zones. The concentration-dependent, transcriptional responses observed here, together with the differences between the gill and hepatopancreas suggest that molecular biomarkers—particularly those related to energy metabolism, immune function, and oxidative stress—could serve as sensitive indicators of SSC stress in bivalves [40]. The identification of specific genes with robust expression changes across multiple concentrations (e.g., DN88965, DN94928) provides candidate biomarkers for future monitoring programmes.

The non-linear concentration-response relationship, with moderate SSC concentrations eliciting stronger transcriptional responses than the highest concentration, high-lights the importance of considering non-monotonic molecular responses in environmental monitoring.

Several limitations of this study should be acknowledged. First, the laboratory based exposure conditions and single time point design (30 days), while carefully controlled to mimic field SSC concentrations and tidal cycles, cannot fully capture the complexity of natural multi stressor environments or the temporal dynamics of gene expression responses. Second, the study focused on two tissues (gill and hepatopancreas), and responses in other tissues (e.g., mantle, adductor muscle) may differ.

Third, the relatively low annotation rate (26.03% in NR), typical of de novo transcriptomes of non-model organisms, limits the functional interpretation of some DEGs. In addition, the de novo assembly had a BUSCO completeness of 73.2% (single-copy: 70.5%; du-plicated: 2.7%; fragmented: 16.3%; missing: 10.5%), which is within the range commonly reported for non-model marine invertebrates but may have reduced the sensitivity of DEG detection. Future studies using a reference genome would further improve transcriptomic resolution.

Fourth, the discordant trends observed for some genes between RNA-seq and qRT-PCR highlight the importance of validation studies and suggest that technical variability between platforms should be considered when interpreting transcriptomic data.

Fifth, all clams, including the 0 mg/L control and the 276–426 mg/L SSC treatments, were purchased as a single batch from a local seafood market near Tongzhou Bay and randomly assigned to treatment groups. Therefore, between-source differences and source-related confounding are not expected to affect the comparisons. A 7-day temporary holding period period is commonly used in bivalve stress experiments and was sufficient for laboratory stabilization, but it may not completely erase prior holding conditions in the market. However, because all groups experienced identical temporary holding and expo-sure conditions, any residual preconditioning should be balanced across treatments. Future studies using longer temporary holding periods or laboratory-reared clams could further validate the present findings.

Sixth, the stability of 18S rRNA as the internal reference gene was not formally evaluated using algorithms such as geNorm or NormFinder. However, the Ct values of 18S rRNA were relatively stable across all samples (mean Ct range: 17.18–19.88), and 18S rRNA is widely used as a reference gene in bivalve qRT-PCR studies. Future studies should include a formal evaluation of reference gene stability.

Seventh, all differential-expression comparisons were made against the 0 mg/L control, which was intended to characterize the overall transcriptional response to suspended sediment stress. We did not perform comparisons of the 286–426 mg/L treatments against the 276 mg/L background SSC. This omission limits our ability to distinguish the effects of background turbidity from those specifically caused by construction-related SSC increments. Therefore, the present conclusions are restricted to the overall effects of SSC stress across the tested gradient, and we no longer claim to quantify construction-related incremental effects. Future studies should include 276 mg/L as an additional reference control to specifically assess construction-related SSC increments.

Eighth, although the gill and hepatopancreas showed clear differences in the number and composition of DEGs, a formal tissue × SSC interaction analysis was not performed. Therefore, the term “tissue-specific” should be interpreted as a descriptive difference be-tween tissues rather than a statistically validated interaction effect. Future studies with a full factorial design would be needed to formally test tissue × SSC interactions.

Ninth, several mechanistic interpretations proposed in this study, including adaptive transcriptional suppression, impairment of the transcriptional machinery, and the involvement of apoptosis, necroptosis, ferroptosis, and inflammatory pathways, are based on transcriptomic enrichment and should be regarded

as hypotheses rather than established mechanisms. Future functional studies are needed to validate these pathways.

Tenth, the TEM analysis in this study focused on the gill epithelium, because it is the primary interface with suspended particles. The hepatopancreas showed a stronger transcriptomic response, but its ultrastructural changes were not examined by TEM. Future studies combining TEM and transcriptomic analyses of the hepatopancreas are needed to fully understand the tissue-specific mechanisms of SSC stress tolerance.

Despite these limitations, future studies should focus on functional validation of the candidate biomarker genes identified here (e.g., DN88965, DN94928) using gene knock-down or knockout approaches, and field based surveys are needed to assess the applicability of these molecular markers under real world environmental conditions. This study provides a multi-tissue transcriptomic characterisation of SSC stress in *M. meretrix*, establishing a foundation for future research on the molecular mechanisms of particle stress tolerance in bivalves.

5. Conclusions

In this study, combined transcriptomic and ultrastructural analyses revealed that SSC stress induces tissue-specific transcriptional reprogramming and dose-dependent cellular damage in *M. meretrix*. The hepatopancreas mounted a broader transcriptional response than the gill, reflecting distinct metabolic and immune strategies. TEM analysis corroborated these findings at the cellular level, showing progressive damage in gill epithelial cells from reversible stress to terminal necrosis. The identified genes with robust expression changes (e.g., DN88965, DN94928) serve as promising candidate biomarkers for monitoring SSC stress. These results provide a foundation for future functional validation and field applications in coastal environmental assessment.

Supplementary Materials: Table S1: Grain size analysis of the sediment; Table S2: Physicochemical parameters of the experimental water; Table S3: qRT-PCR primer information and correlation analysis between RNA-seq and qRT-PCR.

Author Contributions: Conceptualization, X.Z., Y.S. and L.L.; methodology, X.Z., J.L., H.H. and T.Y.;

software, X.Z., H.H. and T.Y.; validation, X.Z., J.L. and M.J.; formal analysis, X.Z., H.H. and T.Y.; investigation, X.Z., J.L., H.H., T.Y. and M.J.; resources, Y.S. and L.L.; data curation, X.Z. and H.H.; writing—original draft preparation, J.L.; writing—review and editing, X.Z., Y.S. and L.L.; visualization, X.Z., H.H. and T.Y.; supervision, Y.S. and L.L.; project administration, Y.S. and L.L.; funding acquisition, Y.S. and L.L.

Funding: This study was funded by research grants from the National Natural Science Foundation of China (No. 41706142).

Institutional Review Board Statement: The animal study protocol was approved by the Animal Ethics Committee of Chinese Academy of Fishery Sciences East China Sea Fisheries Research lnstitute (protocol code 2026-08 and date of approval 2026-01-25). All procedures involving animals were performed in accordance with the guidelines and regulations for the care and use of experimental animals of Chinese Academy of Fishery Sciences East China Sea Fisheries Research lnstitute.

Informed Consent Statement: Not applicable.

Data Availability Statement: The raw RNA-seq reads generated in this study have been deposited in the NCBI Sequence Read Archive (SRA) under BioProject accession number PRJNA1509981. All other data supporting the findings of this study are included in the article and its Supplementary Materials, or are available from the corresponding author upon reasonable request.

Acknowledgments: Not applicable.

Conflicts of Interest: The authors declare no conflicts of interest. The funders had no role in the design of the study; in the collection, analyses, or interpretation of data; in the writing of the manuscript; or in the decision to publish the results.

References

1. Bayne, B.L. The physiology of suspension feeding by bivalve molluscs: An introduction to the Plymouth "TROPHEE" workshop. *J. Exp. Mar. Biol. Ecol.* **1998**, *219*, 1–19. https://doi.org/10.1016/S0022-0981(97)00172-x
2. Wang, J.M.; Ma, N.; Fan, L.L.; Yuan, L.L.; Zhang, H.Y. Research progress on ecotoxicological effects of suspended solids on marine organisms. *Asian Journal of Ecotoxicology* **2024**, *19*, 27–40. https://doi.org/10.7524/AJE.1673-5897.20231027001
3. Song, L.; Yang, G.J.; Wang, N.B.; Guan, S.G.; Liu, G.X.; Wang, B. Effects of suspended solids on the ecology of marine organisms. *Fisheries Science* **2012**, *31*, 444–448. https://doi.org/10.16378/j.cnki.1003-1111.2012.07.002.

4. Erftemeijer, P.L.A.; Lewis, R.R.R. Environmental impacts of dredging on seagrasses: A review. *Mar. Pollut. Bull.* **2006**, *52*, 1553–1572. https://doi.org/10.1016/j.marpolbul.2006.09.006
5. Liu, X.Q.; Fang, J.G.; Bao, Z.M.; Wang, R.C. Research progress on seedling rearing and culture techniques of major economically important species of Veneridae along the coast of China. *Chinese Journal of Zoology* **2003**, *38*, 114-119. https://doi.org/10.13859/j.cjz.2003.04.022.
6. Wang, H.B.; Wang, C.; Zhang, X.F.; Zen, H.X. Effects of salinity and food density on the filtration rate of Meretrix meretrix. *Heilongjiang Fisheries* **2024**, *43*, 250–253.
7. Ward, J.E.; Shumway, S.E. Separating the grain from the chaff: Particle selection in suspension- and deposit-feeding bivalves. *J. Exp. Mar. Biol. Ecol.* **2004**, *300*, 83–130. https://doi.org/10.1016/j.jembe.2004.03.002
8. Yang, G.J.; Song, L.; Wang, N.B.; Liu, Q.M.; Cheng, W.Q.; Cheng, Z.Q. Effects of suspended sediment on growth and filtration rate of juvenile Ruditapes philippinarum. *Journal of Dalian Ocean University* **2013**, *32*, 2097–2103. https://doi.org/10.13292/j.1000-4890.2013.0414.
9. He, Y.Y.; Yang, F.; Wang, H.; Zhen, C.; Liu, D.; Ma, G.F. Effects of suspended sediment on growth and filtration rate of juvenile Ruditapes philippinarum. *Journal of Dalian Ocean University* **2014**, *29*, 156–160.
10. Barillé, L.; Prou, J.; Héral, M.; Razet, D. Effects of high natural seston concentrations on the feeding, selection, and absorption of the oyster *Crassostrea gigas* (Thunberg). *J. Exp. Mar. Biol. Ecol.* **1997**, *212*, 149–172. https://doi.org/10.1016/S0022-0981(96)02756-6
11. Irisarri, J.; Fernández-Reiriz, M.J.; Robinson, S.M.C.; Cranford, P.J.; Labarta, U. Absorption efficiency of mussels *Mytilus edulis* and *Mytilus galloprovincialis* cultured under Integrated Multi-Trophic Aquaculture conditions. *Aquaculture* **2013**, *388–391*, 182–192. https://doi.org/10.1016/j.aquaculture.2013.01.034
12. Liu, G.Y.; He, W.; Shao, M.H.; Zhang, D.H.; Song, Y.X. Experimental study on the acute lethal dose of dredged materials to Chlamys farreri. *Marine Environmental Science* **1998**, 19–23.
13. Ma, M.H.; Gong, Q.; Liu, S.X.; Cheng, H.X.; Song, Y.X. Study on lethal effects of suspended solids on Patinopecten yessoensis. *Marine Environmental Science* **2004**, 46–48.
14. Xie, B.; Lin, Z.H.; He, L. Effects of particle concentration on retention efficiency of Meretrix meretrix, Mercenaria mercenaria and Ruditapes philippinarum. *Progress in Fishery Sciences* **2022**, *43*, 190–198. https://doi.org/10.19663/j.issn2095-9869.20210310001.
15. Wei, W.; Tang, B.J.; Sun, P.; Jiang, Y.Z.; Li, L. Effects of air exposure stress on filtration rate, respiration and excretion of Meretrix meretrix. *Journal of Guangdong Ocean University* **2017**, *37*, 37–42.
16. Xu, Y.; Wu, C.; Jin, J.; Tang, W.; Chang, A.K.; Ying, X. Transcriptome analysis and identification of cadmium-induced oxidative stress response genes in different *Meretrix meretrix* developmental stages. *Animals* **2024**, *14*, 352. https://doi.org/10.3390/ani14020352
17. Li, Y.; Liu, S.; Cheng, H.; Chen, X.; Shen, X.; Cai, Y. Dynamic transcriptome response in *Meretrix meretrix* to Aroclor 1254 exposure. *Ecotoxicol. Environ. Saf.* **2021**, *207*, 111485. https://doi.org/10.1016/j.ecoenv.2020.111485
18. Cao, J.; Wang, B.; Tan, X. Transcriptomic responses of the clam *Meretrix meretrix* to the organophosphorus pesticide (dimethoate). *Ecotoxicology* **2019**, *28*, 539–549. https://doi.org/10.1007/s10646-019-02051-z
19. Han, S.; Zhu, Y.; Fan, Y.R.; Zhang, X.; Hu, H.P.; Wang, E.B.; Liu, L.Y.; Bao, J.M.; Li, L.; Jiang, M. Transcriptomic and WGCNA analysis of immune and antioxidant responses in *Meretrix meretrix* under combined thermal and residual chlorine stress. *Comp. Biochem. Physiol. Part D* **2026**, *58*, 101760. https://doi.org/10.1016/j.cbd.2026.101760
20. Wang, Y.; Zhang, Z.; Chen, S.; Zhang, Y.; Cao, Y.; Peng, Y.; Zhao, J.; Chen, A.; Wu, Y. Integrated biochemical, histological, and transcriptomic analyses reveal dose-dependent effects of sodium

alginate on the physiology of *Meretrix meretrix*. *Sci Rep* **16**, 11588 (2026). https://doi.org/10.1038/s41598-026-41950-0

21. Bernardini, I., Quagliariello, A., Peruzza, L. *et al.* Contaminants from dredged sediments alter the transcriptome of Manila clam and induce shifts in microbiota composition. *BMC Biol.* **2023**, *21*, 234. https://doi.org/10.1186/s12915-023-01741-9
22. Yasa, N.S.; Purnomo, S.J.; Anshory, L.; Murwantoko; Isnansetyo, A.; Handayani, N.S.N. Gene Expression Profiles of HSP70 and HSP90 Genes and Biochemical Responses in Juvenile Abalone, *Haliotis diversicolor squamata* in Response to Total Suspended Solids. *BIO Web Conf.* **2024**, *92*, 01006. https://doi.org/10.1051/bioconf/20249201006
23. Bolger, A.M.; Lohse, M.; Usadel, B. Trimmomatic: A flexible trimmer for Illumina sequence data. *Bioinformatics* **2014**, *30*, 2114–2120. http://doi.org/10.1093/bioinformatics/btu170
24. Grabherr, M.G.; Haas, B.J.; Yassour, M.; et al. Full-length transcriptome assembly from RNA-Seq data without a reference genome. *Nat. Biotechnol.* **2011**, *29*, 644–652. https://doi.org/10.1038/nbt.1883
25. Davidson, N.M.; Oshlack, A. Corset: Enabling differential gene expression analysis for de novo assembled transcriptomes. *Genome Biol.* **2014**, *15*, 410. https://doi.org/10.1186/s13059-014-0410-6
26. Patro, R.; Duggal, G.; Love, M.I.; Irizarry, R.A.; Kingsford, C. Salmon provides fast and bias-aware quantification of transcript expression. *Nat. Methods* **2017**, *14*, 417–419. https://doi.org/10.1038/nmeth.4197
27. Altschul, S.F.; Madden, T.L.; Schäffer, A.A.; et al. Gapped BLAST and PSI-BLAST: A new generation of protein database search programs. *Nucleic Acids Res.* **1997**, *25*, 3389–3402. https://doi.org/10.1093/nar/25.17.3389
28. Kanehisa, M.; Goto, S. KEGG: Kyoto Encyclopedia of Genes and Genomes. *Nucleic Acids Res.* **2000**, *28*, 27–30. https://doi.org/10.1093/nar/28.1.27
29. Bairoch, A.; Apweiler, R. The SWISS-PROT protein sequence database and its supplement TrEMBL in 2000. *Nucleic Acids Res.* **2000**, *28*, 45–48. https://doi.org/10.1093/nar/28.1.45
30. Huerta-Cepas, J.; Szklarczyk, D.; Heller, D.; et al. eggNOG 5.0: A hierarchical, functionally and phylogenetically annotated orthology resource based on 5090 organisms and 2502 viruses. *Nucleic Acids Res.* **2019**, *47*, D309–D314. https://doi.org/10.1093/nar/gky1085
31. Haas, B.J.; Papanicolaou, A.; Yassour, M.; et al. De novo transcript sequence reconstruction from RNA-seq using the Trinity platform for reference generation and analysis. *Nat. Protoc.* **2013**, *8*, 1494–1512. https://doi.org/10.1038/nprot.2013.084
32. Robinson, M.D.; McCarthy, D.J.; Smyth, G.K. edgeR: a Bioconductor package for differential expression analysis of digital gene expression data. *Bioinformatics* **2010**, *26*, 139–140. https://doi.org/10.1093/bioinformatics/btp616
33. Yang, Y.H.; Paquet, A. *goTools: Functions for Gene Ontology database*. R package version 0.9.9. https://bioconductor.org/packages/goTools
34. Xie, C.; Mao, X.; Huang, J.; et al. KOBAS 2.0: a web server for annotation and identification of enriched pathways and diseases. *Nucleic Acids Res.* **2011**, *39*, W316–W322. https://doi.org/10.1093/nar/gkr483
35. Livak, K.J.; Schmittgen, T.D. Analysis of relative gene expression data using real-time quantitative PCR and the $2^{-}\Delta\Delta Ct$ method. *Methods* **2001**, *25*, 402–408. https://doi.org/10.1006/meth.2001.1262
36. Liu, Z.; Zhang, H.; Lai, C.; Sun, R.; Xu, H.; Yao, H.; Dong, Y.; Lin, Z.; Lv, L. Synergistic Effects of Ammonia and Hypoxia Stress on the Transcriptomic Responses of the Razor Clam (Sinonovacula constricta). Animals **2026**, *16*, 896. https://doi.org/10.3390/ani16060896
37. Xue, C.; Xu, K.; Jin, Y.; Bian, C.; Sun, S. Transcriptome Analysis to Study the Molecular Response in the Gill and Hepatopancreas Tissues of Macrobrachium nipponense to Salinity Acclimation. Front. Physiol. **2022**, *13*, 926885. https://doi.org/10.3389/fphys.2022.926885

38. Zhang, R.; Shi, X.; Liu, Z.; et al. Histological, Physiological and Transcriptomic Analysis Reveal the Acute Alkalinity Stress of the Gill and Hepatopancreas of *Litopenaeus vannamei*. *Mar. Biotechnol.* **2023**, *25*, 588–602. https://doi.org/10.1007/s10126-023-10228-1
39. Park, S.Y.; Lee, J.; Byeon, Y.; Khim, J.S. Systematic review of suspended sediment effects on aquatic organisms across taxa, developmental stages, and endpoints. *Mar. Pollut. Bull.* **2025**, *221*, 118568. https://doi.org/10.1016/j.marpolbul.2025.118568
40. Asnicar, D.; Fabrello, J.; Ciscato, M.; Masiero, L.; Marin, M.G.; Corami, F.; Milan, M.; Bernardini, I.; Patarnello, T.; Cecchetto, M.; et al. A multibiomarker approach in clams (*Ruditapes philippinarum*) for a toxicological evaluation of dredged sediments. *Environ. Pollut.* **2024**, *342*, 123095. https://doi.org/10.1016/j.envpol.2023.123095
41. Amorim, K.; Piontkivska, H.; Zettler, M.L.; Sokolov, E.; Hinzke, T.; Nair, A.M.; Sokolova, I.M. Transcriptional response of key metabolic and stress response genes of a nuculanid bivalve, *Lembulus bicuspidatus* from an oxygen minimum zone exposed to hypoxia-reoxygenation. *Comp. Biochem. Physiol. Part B* **2021**, *256*, 110617. https://doi.org/10.1016/j.cbpb.2021.110617
42. Adzigbli, L.; Ponsuksili, S.; Sokolova, I. Mitochondrial responses to constant and cyclic hypoxia depend on the oxidized fuel in a hypoxia-tolerant marine bivalve *Crassostrea gigas*. *Sci. Rep.* **2024**, *14*, 9658. https://doi.org/10.1038/s41598-024-60261-w
43. Wu, X.; Li, Y.; Yan, B.; Liu, Y.; Li, H.; Chen, M.; Deng, J.; Xu, C.; Zhang, H.; Zheng, H. Identification and analysis of caspase genes in bivalves and their expression patterns in noble scallop *Chlamys nobilis* under low-temperature stress. *Fish Shellfish Immunol.* **2025**, *166*, 110655. https://doi.org/10.1016/j.fsi.2025.110655
44. Falfushynska, H.; Piontkivska, H.; Sokolova, I.M. Effects of intermittent hypoxia on cell survival and inflammatory responses in the intertidal marine bivalves *Mytilus edulis* and *Crassostrea gigas*. *J. Exp. Biol.* **2020**, *223*, jeb217026. https://doi.org/10.1242/jeb.217026
45. Zuo, S.; Jiang, K.; Li, D.; Yan, X.; Nie, H. Transcriptomic analysis of Manila clam *Ruditapes philippinarum* under lipopolysaccharide challenge provides molecular insights into immune response. *Fish Shellfish Immunol.* **2020**, *106*, 110–119. https://doi.org/10.1016/j.fsi.2020.07.022
46. Wei, B.; Wang, H.; Dong, Z.; Xin, Z.; Zhang, W.; Lin, H.; Wang, W.; Song, M.; Guo, B. Transcriptomic analysis reveals the survival strategies of *Mytilus coruscus* under short-term rising seawater temperatures. *Comp. Biochem. Physiol. Part D* **2025**, *55*, 101481. https://doi.org/10.1016/j.cbd.2025.101481
47. Dou, M.; Jiao, Y.H.; Zheng, J.W.; Zhang, G.; Li, H.Y.; Liu, J.S.; Yang, W.D. De novo transcriptome analysis of the mussel *Perna viridis* after exposure to the toxic dinoflagellate *Prorocentrum lima*. *Ecotoxicol. Environ. Saf.* **2020**, 192, 110265. https://doi.org/10.1016/j.ecoenv.2020.110265

Supplementary Files

This is a list of supplementary files associated with this preprint. Click to download.

- SupplementaryFiles.zip